Reactivity Paradigms: Transition State Structure, Mechanisms of Barrier Formation, and Stereospecificity of Nucleophilic Substitutions on σ-Cation Radicals

Sason Shaik,*[1a] A. Chandrasekhar Reddy,*[1a] Alexander Ioffe,[1a] Joseph P. Dinnocenzo,[1b] David Danovich,[1a] and Jeoung Ki Cho[1c]

Contribution from the Department of Organic Chemistry and the Fritz Haber Center of Molecular Dynamics, The Hebrew University, 91904 Jerusalem, Israel, and the Department of Chemistry, The University of Rochester, Rochester, New York 14627

Received April 21, 1994[⊗]

Abstract: The present work is concerned with odd electron reactivity *and uses ab initio computations and VB mixing modeling to develop effective means for conceptualizing and predicting reactivity patterns in the nucleophilic substitution reactions on σ-cation radicals.* All critical species along the reaction profile were characterized for both the *backside* and *frontside* substitution pathways. The backside and frontside transition states (TSs) in the case of $H_2S + C_2H_6^{\bullet+}$ were located also in two solvents. The computational data were then processed by a VB analysis which *models the state of the reaction complex along the entire reaction profile in terms of the contributing VB configurations.* Subsequently, the VB information was converted into VB mixing diagrams and reactivity paradigms were formulated. The resulting analysis provides insight *into the electronic structure and bonding in the TS as well as into the origins of the barrier and stereospecificity in nucleophilic substitutions on cation radicals.* Mechanistic predictions are made and isotope effect probes developed for the stereochemistry and the electronic structure of the TSs.

Introduction

Effective paradigms are needed to guide the generation and solution of chemical problems. For reactions that involve an even number of electrons, several MO paradigms played a key role in the Renaissance of organic reactivity studies, e.g., the Woodward−Hoffmann (WH) rules[2] and frontier molecular orbital FMO) theory.[3] For reactions that involve an odd number of electrons, the insight provided by these qualitative MO models is much less decisive. Indeed, WH rules have not been developed for odd-electron reactions, for the same reason that Hückel rules do not apply for odd-electron systems. Similarly, FMO theory does not provide definitive predictions for important features of odd-electron reactions such as regioselectivity and stereoselectivity.[4] Valence bond mixing and curve crossing ideas[5] which deal directly with mechanisms of barrier formation have the potential to provide a general and predictively useful model for odd-electron reactions. The present work shows how these ideas can be developed to provide insight into a particular set of odd-electron reactions: nucleophilic substitutions on σ-cation radicals.[6] Other reactivity patterns of cation radicals and nucleophiles, especially electron- and proton transfer reactions will be addressed in the future.

To set the background, we first review briefly some major issues and controversies in the field of reactivity of nucleophiles toward cation radicals. Early observations[7] that cation radicals are sometimes persistent in a nucleophilic environment have repeatedly drawn the attention of investigators in the area.[8] Eberson analyzed the problem and concluded that cation radicals react more sluggishly than simple cations with nucleophiles.[9] In 1986 Pross[10] used curve crossing ideas to analyze the relative reactivity of a cation radical toward a nucleophile and compared it with that of a simple cation. He concluded that the reaction of a cation radical with a nucleophile is comparatively sluggish because the excited state in the curve crossing diagram involves "double excitation" with respect to the ground state of the nucleophile/cation radical pair. His conclusions provided support for Eberson's analysis but went a step further to suggest that the reactions may be classified as "forbidden" because of the double excitation involved in the formation of the barrier. This prediction was followed by a series of critical papers by Schwarz and co-workers[11] and by Parker and Tilset[12] who showed that reactions of cation radicals with nucleophiles can

⊗ Abstract published in *Advance ACS Abstracts,* February 1, 1995.

(1) (a) The Hebrew University. (b) The University of Rochester. (c) Current address: Man-Su Z Dong 80-257, Inchoen 405-242, South Korea.

(2) Woodward, R. B.; Hoffmann, R. *The Conservation of Orbital Symmetry*; Academic Press: New York, 1970.

(3) Fukui, K. *Theory of Orientation and Stereoselection*; Wiley-Interscience: New York, 1976.

(4) At the simplest qualitative level, the number of electrons (two vs three) will prefer the HOMO−LUMO interaction, while the energy gap factor will prefer the HOMO−SOMO factor. The latter interaction becomes repulsive for large overlaps.

(5) (a) Shaik, S. S. *J. Am. Chem. Soc.* **1981**, *103*, 3692. (b) Pross, A.; Shaik, S. S. *Acc. Chem. Res.* **1983**, *16*, 363. (c) Shaik, S. S. *Progr. Phys. Org. Chem.* **1985**, *15*, 197. (d) Pross, A. *Adv. Phys. Org. Chem.* **1985**, *21*, 99. (e) Shaik, S. S.; Schlegel, H. B.; Wolfe, S. *Theoretical Aspects of Physical Organic Chemistry. The S_N2 Mechanism*; Wiley and Sons: New York, 1992.

(6) (a) Dinnocenzo, J. P.; Todd, W. P.; Simpson, T. R.; Gould, I. R. *J. Am. Chem. Soc.* **1990**, *112*, 2462. (b) Dinnocenzo, J. P.; Farid, S.; Goodman, J. L.; Gould, I. R.; Todd, W. P.; Mattes, S. *J. Am. Chem. Soc.* **1989**, *111*, 8973. (c) Rao, V. R.; Hixson, S. S. *J. Am. Chem. Soc.* **1979**, *101*, 6548. (d) Gassman, P. G.; Olson, K. D. *J. Am. Chem. Soc.* **1982**, *104*, 3740. (e) Gassman, P. G.; Hay, B. A. *J. Am. Chem. Soc.* **1986**, *108*, 4227. (f) Mazzocchi, P. H.; Somich, C.; Edwards, M.; Morgan, T.; Ammon, H. L. *J. Am. Chem. Soc.* **1986**, *108*, 6828. (g) Du, X.; Arnold, D. R.; Boyd, R. J.; Shi, Z. *Can. J. Chem.* **1991**, *69*, 1365.

(7) (a) Bard, A. J.; Ledwith, A.; Shine, H. J. *Adv. Phys. Org. Chem.* **1976**, *12*, 155. (b) Hammerich, O.; Parker, V. D. *Adv. Phys. Org. Chem.* **1984**, *20*, 55. (c) Parker, V. D. *Acc. Chem. Res.* **1984**, *17*, 243. (d) Evans, J. F.; Blount, H. N. *J. Am. Chem. Soc.* **1978**, *100*, 4191. (e) Silber, J. J.; Shine, H. J. *J. Org. Chem.* **1971**, *36*, 2923.

(8) For a summary, see: Eberson, L. *Electron Transfer Reactions in Organic Chemistry*; Springer-Verlag: Heidelberg, 1987 (especially pp 94−97).

(9) (a) Eberson, L.; Nyberg, K. *Acta Chem. Scand.* **1978**, *B32*, 235. (b) Eberson, L.; Blum, Z.; Helge, B.; Nyberg, K.; *Tetrahedron* **1978**, *34*, 731.

(10) Pross, A. *J. Am. Chem. Soc.* **1986**, *110*, 3537.

0002-7863/95/1517-3205$09.00/0

be very fast. In 1989, Shaik and Pross[13] reconsidered the problem based on a semiquantitative analysis of the curve crossing model and showed that double excitation can often be quite small and thereby give rise to small reaction barriers. Following that, Grutzmacher and collaborators[14] found several inefficient gas phase reactions of nucleophiles with arene cation radicals that exhibited a remarkable isomer selectivity, which was explained by a clever articulation[14a] of the curve crossing model. Despite the somewhat balanced situation, it has remained unclear how to use the VB curve crossing model to account for the reactivity of cation radicals toward nucleophiles, i.e., how to predict reactivity patterns and reaction rates and, furthermore, how these depended on the nature of the nucleophile and the cation radical.

Another application of the VB curve crossing model appeared in 1990 by Shaik and Dinnocenzo[15] who showed that the inversion of configuration observed in the nucelophilic cleavage of σ-cation radicals[6a] can be accounted for by use of VB configurations based on reactant fragment orbitals. According to the model, "the stereochemical course of nucleophilic displacement of one-electron σ bonds will be governed by the σ^* (LUMO) orbital of the one electron bond and will therefore proceed with inversion of configuration at the site of attack".[15] This prediction demonstrated that the VB model was capable of unraveling the complex orbital interactions and singling out a dominant contribution that governs the stereochemistry. Further support for this analysis has been provided by a recent experimental study by Eberson and Radner[16] and Eberson et al.[17] who used the "*nonalternant hydrocarbon test*" to demonstrate that nucleophilic attack on the dibenzofuran cation radical occurs at the site of the highest coefficient in the LUMO of the cation radical as well as the site of the highest triplet spin density of the neutral nonalternant hydrocarbon as predicted by the VB model. However, a counter example also exists from the theoretical study of Schwarz et al.[18] who argued that the regioselectivity of nucleophilic attack of NH_3 on the ketene cation radical is in line with the SOMO coefficients of the cation radical. Our own calculations[19] of the $NH_3/C_2H_2O^{\bullet+}$ system show that the observed regioselectivity follows the site of the highest triplet spin density of the neutral ketene, which coincides with the highest SOMO coefficient. Thus, the VB model appears to possess a unique predictive ability in these particular aspects of chemical reactivity.

Clearly, the reactions of cation radicals with nucleophiles is a multidimensional problem involving relative rates, structural aspects like stereoselectivity[6,15] and regioselectivity[16-19] as well as intriguing substituent effects.[20] This and the unresolved controversies surrounding the applicability of the VB curve crossing model make the task extremely fascinating and demanding. We need an effective paradigm that can be applied in the area of cation radical/nucleophile reactivity in a rigorous and yet chemically lucid manner, and the VB model has the potential to be such an effective tool after some refinement. This is the major goal of the present paper which is achieved by coupling the VB analysis to ab initio computations of transition states (TSs) and barrier heights for these reactions.[21]

The present study is focused on the ab initio computations and VB modeling of nucleophilic cleavages of σ-cation radicals using the model systems in eqs 1 and 2.

$$\text{Nu:} + M_2H_6^{\bullet+} \rightarrow {}^{+}\text{Nu-}MH_3 + MH_3^{\bullet} \qquad (1)$$

$$\text{Nu:} = H_2S,\ H_2O,\ NH_3,\ PH_3;\ M = C,\ Si$$

$$\text{Nu:} + C_3H_6^{\bullet+} \rightarrow {}^{+}\text{Nu-}CH_2CH_2CH_2^{\bullet} \qquad (2)$$

$$\text{Nu:} = H_2S,\ H_2O,\ NH_3$$

These cation radicals,[22-25] and especially $C_2H_6^{\bullet+}$,[22] are known to possess a few electron-shift isomers[23b] of differing stabilities. Since our goal was to model nucleophilic cleavages of one-electron bonds, the present study was limited to the long-bond isomers where the one-electron bond is of the C−C[23b,c,24] or Si−Si[23c] variety. The computations were designed to address two central mechanistic questions: (a) What is the mechanism and stereochemistry of the nucleophilic substitution of one-electron bonds, and how can these features be probed by experimental means? (b) Are the reaction barriers small or large, and how do they depend on the nature of the nucleophile and cation radical?

Our strategy of formulating an effective theoretical model involves two key steps. In the first step, VB features are extracted directly from the computational charge and spin density data. This analysis[21] allows us to model the state of the reaction complex along the entire reaction profile in terms of the contributing VB configurations. In the second step, the VB information is converted into VB mixing models, and reactivity paradigms are formulated. The resulting scheme addresses the questions posed above and provides *insight into the electronic structure and bonding in the TS, into the origins of the barrier and stereospecificity in nucleophilic cleavage reactions of cation radicals as well as to the possible experimental probes of these aspects.*

Theoretical Methods and Calculations

A. Computational Details. Programs. Most of the computations were performed with the GAUSSIAN-92 (REV-C3) series of pro-

(11) Drewello, T.; Heinrich, N.; Mass, W. M. P.; Nibbering, N. M. M.; Weiske, T.; Schwarz, H. *J. Am. Chem. Soc.* **1987**, *109*, 4810.

(12) (a) Parker, V. D.; Tilset, M. *J. Am. Chem. Soc.*, **1987**, *109*, 2521. (b) Parker, V. D.; Tilset, M. *J. Am. Chem. Soc.* **1987**, *110*, 1649.

(13) Shaik, S. S.; Pross, A., *J. Am. Chem. Soc.* **1989**, *111*, 4306.

(14) (a) Tholman, D.; Grutzmacher, H.-Fr. *J. Am. Chem. Soc.* **1991**, *113*, 3281. (b) Tholman, D.; Floattmann, D.; Grutzmacher, H.-Fr. *Chem. Ber.* **1991**, *124*, 2349.

(15) Shaik, S. S.; Dinnocenzo, J. P. *J. Org. Chem.* **1990**, *55*, 3434.

(16) (a) Eberson, L.; Radner, F. *Acta. Chem. Scand.* **1992**, *46*, 802. (b) Eberson, L.; Radner, F. *Acta. Chem. Scand.* **1992**, *46*, 312.

(17) Eberson, L.; Hartshorn, M. P.; Radner, F.; Merchan, M.; Roos, B. O. *Acta. Chem. Scand.* **1993**, *47*, 176.

(18) Heinrich, N.; Koch, W.; Morrow, J. C.; Schwarz, H. *J. Am. Chem. Soc.* **1988**, *110*, 6332.

(19) (a) Shaik, S.; Ioffe, A., unpublished. CASSCF (full π space)//UHF/3-21G calculations show that the highest triplet spin density of $\pi\pi^*$ triplet ketene resides on the CH_2 terminus which also has the highest HOMO coefficient in the ground state ketene and the highest SOMO coefficient in the cation radical ketene. We note that the site with the highest LUMO coefficient is disfavored due to instability of the respective addition product. (b) For the analysis of regioselectivity in radical addition to olefins and for the identity of the site with the highest triplet spin density to the site with the highest HOMO density, see: Shaik, S. S.; Canadell, E. *J. Am. Chem. Soc.* **1990**, *112*, 1446.

(20) Dinnocenzo, J. P.; Lieberman, D. R.; Simpson, T. R. *J. Am. Chem. Soc.* **1993**, *115*, 366.

(21) For a related strategy, see: Shaik, S.; Ioffe, A.; Reddy, A. C.; Pross, A. *J. Am. Chem. Soc.* **1994**, *116*, 262.

(22) Bouma, W. J.; Poppinger, D.; Radom, L. *Isr. J. Chem.* **1983**, *23*, 21.

(23) (a) Lunell, S.; Huang, M. B. *J. Chem. Soc. Chem. Commun.* **1989**, 1031. (b) Ioffe, A.; Shaik, S. S. *J. Chem. Soc., Perkin Trans. 2* **1993**, 1461. (c) Clark, T. *J. Am. Chem. Soc.* **1988**, *110*, 1672. (d) Bellville, D. J.; Bauld, N. L. *J. Am. Chem. Soc.* **1982**, *104*, 5700. (e) Bellville, D. J.; Pabon, R. A.; Bauld, N. L. *J. Am. Chem. Soc.* **1985**, *107*, 4978.

(24) (a) Pu, P.; Harovat, D. A.; Borden, W. T. *J. Am. Chem. Soc.* **1988**, *110*, 3405. (b) Lunell, S.; Eriksson, L. A.; Huang, M.-B. *J. Mol. Struct. (THEOCHEM)* **1991**, *23*, 363. (c) Eriksson, L. A.; Lunell, S. *J. Am. Chem. Soc.* **1992**, *114*, 4532. (d) Wayner, D. D. M.; Boyd, R. J.; Arnold, D. R. *Can. J. Chem.* **1983**, *61*, 2310. (e) Hudson, C. E.; Giam, C. S.; McAdoo, D. J. *J. Org. Chem.* **1993**, *58*, 2017. (f) Jespersen, K. K.; Roth, H. D. *J. Am. Chem. Soc.* **1992**, *114*, 8388.

(25) Curtiss, L. A.; Raghavachari, K.; Duetch, P. W.; Pople, J. A. *J. Chem. Phys.* **1991**, *95*, 2433.

grams[26] on an RS/6000 Workstation. The critical points for the reactions of H_2S with $C_2H_6^{\bullet+}$ were initially located with the GAUSSIAN-90 (REV-J) series of programs,[27] but all subsequent work was done with the GAUSSIAN-92 package. Earlier results[28] with the 3-21G* and 3-21G*(d) basis sets were obtained with the GAUSSIAN-88 suit of programs.[29] Vertical charge transfer and triplet states in the avoided crossing diagram were calculated using GAMESS-93.[30] The vertical species is calculated first, and its orbital occupation is inspected. If required, the orbital occupation is altered by guess alteration, and the SCF procedure is made to converge at the desired electronic structure by use of the keyword, DAMP = FALSE, RSTRCT = TRUE.

Basis Sets, Geometry Optimizations, and Computational Levels. The standard basis set used in most of the ab initio calculations is 6-31G*. Earlier calculations used the 3-21G* and 3-21G*(d) basis sets, where the latter involves the d-type polarization functions taken from the 6-31G* basis set for the first row atoms.[28]

The geometries of all the critical species were optimized by gradient methods and checked by frequency calculations, while reaction pathways were ascertained by use of IRC options.[31] The geometric search for the reaction of H_2O with $C_2H_6^{\bullet+}$ was carried out at the HF (UHF for open shell and RHF for closed shell) and the MP2 (UMP2 and RMP2) levels.

The energies of the critical points were determined at correlated levels up to QCISD(T). Shorthand standard notations are used to characterize the computational procedure. For example, QCISD(T)/UMP2/6-31G* refers to QCISD(T) energy determined at the geometry optimization level of UMP2 with the 6-31G* basis set. Projected wave functions and energies[32] were also obtained and are indicated in the customary manner, e.g., PUMP2 means a projected UMP2 level. The signifier FC, e.g., MP2(FC), refers to the frozen core approximation, in which the correlation calculation excludes inner core electrons. Without this signifier, the correlation calculation includes also the core electrons.

Solvent Effect. The transition states (TSs) for the cleavage of $C_2H_6^{\bullet+}$ by H_2S were reoptimized at the SCRF level which incorporates the reaction field solvation model in the SCF procedure.[33] The solute's cavity radius was computed from the gas phase structure, using the recommended practice of adding 0.5 Å to the radius calculated from the electron density of the molecular species (keyword = Volume). The dielectric constants were taken from standard sources and correspond to the values at T = 293 K. The SCRF/UHF geometry optimization follows the standard optimization procedures described above. The shorthand notation used to characterize these calculations includes the SCRF acronym, e.g., SCRF/UHF//6-31G* refers to a UHF optimization level coupled with the SCRF solvation procedure and the 6-31G* basis set. SCRF calculations provide, of course, a very limited view of solvation, and the results should be viewed within this context as a perturbation of the gas phase surface by an interaction of the molecular system with a dipole.

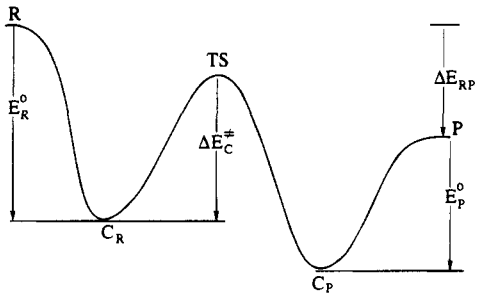

Figure 1. A characteristic double well reaction profile for the cleavage of a σ-cation radical by a nucleophile. Indicated on the profile are R (reactants), C_R (reactant cluster), TS (transition state), C_p (product cluster), and P (products). The $\Delta E_C^{\ddagger}$ is the central barrier.

Isotope Effects. Classical isotope effects were calculated using free energies in Eyring's equation. Scaled (by 0.8929)[26] as well as unscaled vibrational frequencies and entropies were used to evaluate the thermodynamic contributions required for the calculations of the isotope effects.

Spin and Charge Densities. Construction of a VB Model. Group charges and spin densities were assigned based on Mulliken population analysis, using the unprojected as well as projected[32] wave functions up to QCISD(T) level. Obtaining the projected wave functions requires a nonstandard route that is accessed by the keyword iop(5/14=2) in GAUSSIAN-92. The QCISD(T) densities are corrected to second order.

These charges and spin densities were converted in turn to coefficients of the contributing VB structures (see later, **1**−**4**) in a model wave function (see eqs 4−8).[34] The performance of the model wave function is uniformly very good for all the critical structures on the potential energy profile. It is noted that the Mulliken population analysis is just one of the many methods for obtaining charges and spin densities, and it is entirely possible to couple the procedure to any population partition scheme.

B. Reliability of the Computations. In terms of the major goals of the present paper, the key conclusions concerning the stereochemistry of the nucleophilic cleavage step[35] and the nature of the TS are reliable already at the UHF level of optimization (see later). We note that the UMP2 level emphasizes the electron transfer character of the wave function. Indeed, QCISD(T) wave functions were invariably found to be very close to the UHF wave function, and quite different than the UMP2 wave functions. For this reason, we rely on the QCISD(T) or UHF wave functions throughout this study.

Results

Figure 1 is a characteristic double-well reaction profile that describes the backside as well as the frontside nucleophilic cleavages of the target σ-cation radicals $M_2H_6^{\bullet+}$ (M = C, Si) and $C_3H_6^{\bullet+}$, in eqs 1 and 2 above. The reaction profile generally involves a reactant-type cluster, C_R, which precedes a substitution TS. In all the cases involving $M_2H_6^{\bullet+}$ (M = C, Si), a product-type ion-diple cluster, Cp, succeeds the TS, while in the reactions of $C_3H_6^{\bullet+}$ there is no product cluster, and the product is a distonic cation radical of the general type, $^+NuCH_2CH_2CH_2^{\bullet}$.

(26) Frisch, M. J.; Trucks, G. W.; Head-Gordon, M.; Gill, P. M. W.; Wong, M. W.; Foresman, J. B.; Johnson, B. G.; Schlegel, H. B.; Robb, M. A.; Replogle, E. S.; Gomperts, R.; Andres, J. L.; Raghavachari, K.; Binkley, J. S.; Gonzalez, C.; Martin, R. L.; Fox, D. J.; Defrees, D. J.; Baker, J.; Stewart, J. J. P.; Pople, J. A. *Gausian 92, Revision C3*; Gaussian, Inc., Pittsburgh, PA, 1992.

(27) Frisch, M. J.; Head-Gordon, M.; Trucks, G. W.; Foresman, J. B.; Schlegel, H. B.; Raghavachari, K.; Robb, M.; Binkley, J. S.; Gonzalez, C.; Defrees, D. J.; Fox, D. J.; Whiteside, R. A.; Seeger, R.; Melius, C. F.; Baker, J.; Martin, R. L.; Kahn, L. R.; Stewart, J. J. P.; Topiol, S.; Pople, J. A. *Gaussian 90, Revision J*; Gaussian, Inc.: Pittsburgh, PA, 1990.

(28) Cho, J. K.; Shaik, S. *J. Am. Chem. Soc.* **1991**, *113*, 9890.

(29) Frisch, M. J.; Head-Gordon, M.; Schlegel, H. B.; Raghavachari, K.; Binkley, J. S.; Gonzales, C.; DeFrees, D. J.; Fox, D. J.; Whiteside, R. A.; Seeger, R.; Melius, R.; Baker, J.; Martin, R.; Stewart, J. J. P.; Fluder, E. M.; Topiol, S.; Pople, J. A. *Gaussian 88*; Gaussian, Inc., Pittsburgh, PA 15213.

(30) GAMESS-93; Schmidt, M. W.; Baldrige, K. K.; Boatz, J. A.; Jensen, J. H.; Koseki, S.; Gordon, M. S.; Nguyen, K. A.; Windus, T. L.; Elbert, S. T. *QCPE Bulletin*; **1990**, *10*, 52−45, revision 11 March 1993.

(31) (a) Gonzalez, C.; Schlegel, H. B. *J. Chem. Phys.* **1989**, *90*, 2154. (b) Gonzalez, C.; Schlegel, H. B. *J. Phys. Chem.* **1990**, *94*, 5523.

(32) (a) Schlegel, H. B. *J. Chem. Phys.* **1986**, *84*, 4530. (b) Gonzalez, C.; Sosa, C.; Schlegel, H. B.; *J. Phys. Chem.* **1989**, *93*, 2435.

(33) Wong, M. H.; Frisch, M. J.; Wiberg, K. B. *J. Am. Chem. Soc.* **1991**, *113*, 4776.

(34) For an alternative VB analysis of MO based wavefunctions, see: (a) Hiberty, P. C.; Leforestier, C. *J. Am. Chem. Soc.* **1978**, *100*, 2012. (b) Hiberty, P. C. *Int. J. Quant. Chem.* **1981**, *XIX*, 259.

(35) As a result of the competition between nucleophilic cleavage and electron transfer characters, it is possible to characterize bond cleavage TSs of two kinds. The first kind of substitution TS involves a nucleophilic attack on the cation radical moiety, e.g., $C_2H_6^{\bullet+}$, while the second type involves a *radical attack* of a $Nu^{\bullet+}$ on the neutral substrate, e.g., C_2H_6. Radical attack type TSs were found for $NH_3/C_2H_6^{\bullet+}$ and $PH_3/C_2H_6^{\bullet+}$ at the UHF level as well as for $H_2S/C_2H_6^{\bullet+}$ during a UMP2 geometry optimization. These mechanisms as well as electron transfer and proton abstraction mechanisms are discussed in a separate work submitted elsewhere (Reddy, A. C.; Danovich, D.; Ioffe, A.; Shaik, S. *J. Chem. Soc., Perkin Trans. 2*, in press).

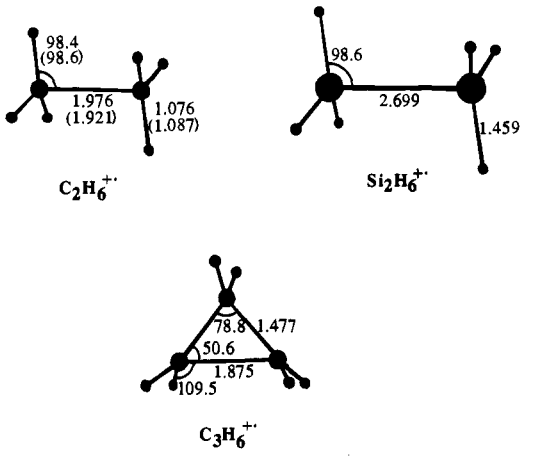

Figure 2. UHF/6-31G* optimized geometries of the long-bond isomers of the reactant cation radicals described in eqs 1 and 2. The parenthetical values for $C_2H_6^{\bullet+}$ are UMP2/6-31G* optimized.

A. Structural Results. Reactants. The reactant cation radicals are shown in detail in Figure 2 and correspond to the isomers that possess a one-electron σ-bond between the heavy atoms. The long-bond structures for $C_2H_6^{\bullet+}$,[22,23] $C_3H_6^{\bullet+}$,[22,24] and $Si_2H_6^{\bullet+}$ [23c,25] are well documented and in the present study serve to model nucleophilic cleavages of one-electron σ-bonds.

Transition States (TSs). The nucleophilic cleavage TSs come in two structural types, backside and frontside, as indicated schematically in Figure 3. The principal skeletal geometric parameters for all the critical species of the backside and frontside mechanisms are summarized in Tables 1–3, and a few cases are shown in detail in Figures 4 and 5. The full geometric parameters are available from the authors in a form of a GAUSSIAN archive.

Figure 4 uses the structural data of Tables 1 and 2 to display the backside and frontside TSs of the nucleophilic cleavage mechanisms of $C_2H_6^{\bullet+}$ by H_2S in the gas phase and in two solvents and by H_2O in the gas phase (from the entries 2b). As may be seen, the frontside TSs possess longer Nu–C_1 and C_1–C_2 distances and a much larger HC_1C_2 in-plane angle in the cation radical ($\beta \sim 130°$ vs $\sim 90°$, see also Tables 1 and 2). These trends as well as the overlap population information indicate inferior Nu–C_1 bonding and greater C_1–C_2 bond breaking in the frontside TSs relative to their backside counterparts.

The $C_2H_6^{\bullet+}/H_2S$ TSs in solvents (Figure 4a,b) are seen to be more advanced relative to the gas phase in terms of Nu–C_1 bond-making and C_1–C_2 bond-breaking. However, the principal differences between the backside and frontside TSs are retained also in solution.

Figure 5 displays the TS data for the reactions of H_2S and H_2O with $C_3H_6^{\bullet+}$. Again, the frontside TSs are seen to be loosely bonded and to possess more C_1–C_2 bond breaking relative to the backside isomers, albeit the differences are now less extreme in comparison with the $C_2H_6^{\bullet+}$ system.

Figures 4 and 5 also reveal an interesting structural trend, namely the dependence of the TS structure on the nature of the nucleophile. Consider, for example, the inclination angle α between the HNuH bisector and the Nu–C_1 bond in the backside TSs in Figure 4. This angle indicates that, in comparison with H_2O, the H_2S assumes an orientation that is better suited for overlap between the nucleophilic p-orbital and the p(σ)-type orbitals along the C_1–C_2 axis. The calculated cost of forcing the $C_2H_6^{\bullet+}/H_2O$ TS to assume the same inclination angle α as in the $C_2H_6^{\bullet+}/H_2S$ TS raises the energy of the $C_2H_6^{\bullet+}/H_2O$ by 5.2 kcal/mol and indicates that this is a significant feature which distinguishes the two TSs. There are also important differences in the overlap populations. Thus, in contrast to the significant S–C_1 overlap population in the TS of H_2S (0.09), the H_2O case possesses a negative O–C_1 overlap population (−0.002) at the UHF level (or marginally positive (0.01) at the UMP2 level).

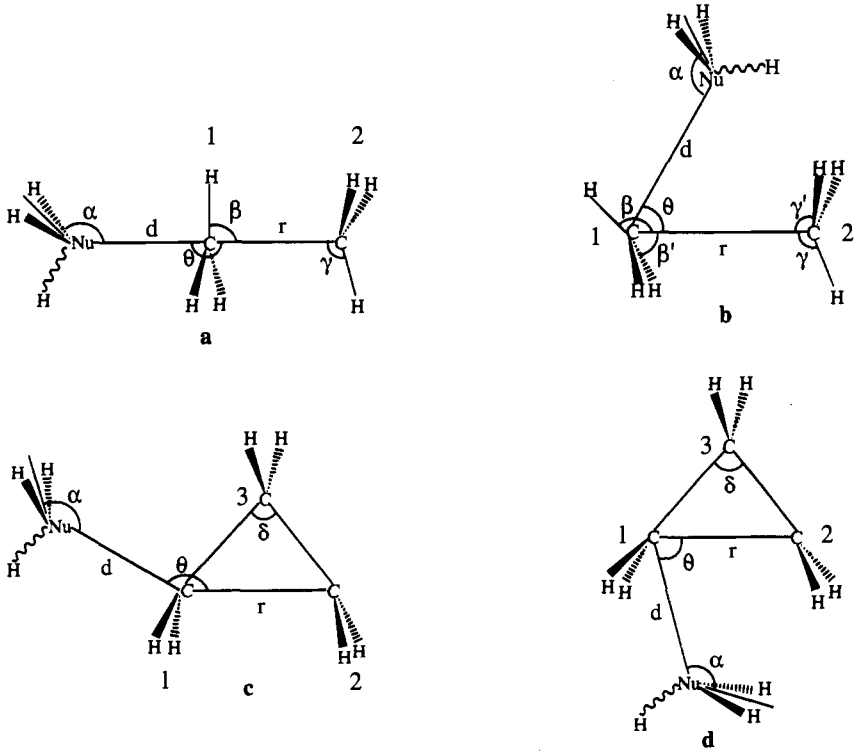

Figure 3. Schematic representations of the backside and frontside structures for the reactions in eqs 1 and 2 (using M = C). The wiggly line connecting Nu to H means that this H is present only in nucleophiles like NH_3 but absent in nucleophiles like H_2S. Principal geometric parameters are indicated on the structures. The cation radical groups are numbered as 1, 2, and 3: 1 corresponds to the site of attack and 2 to the leaving group.

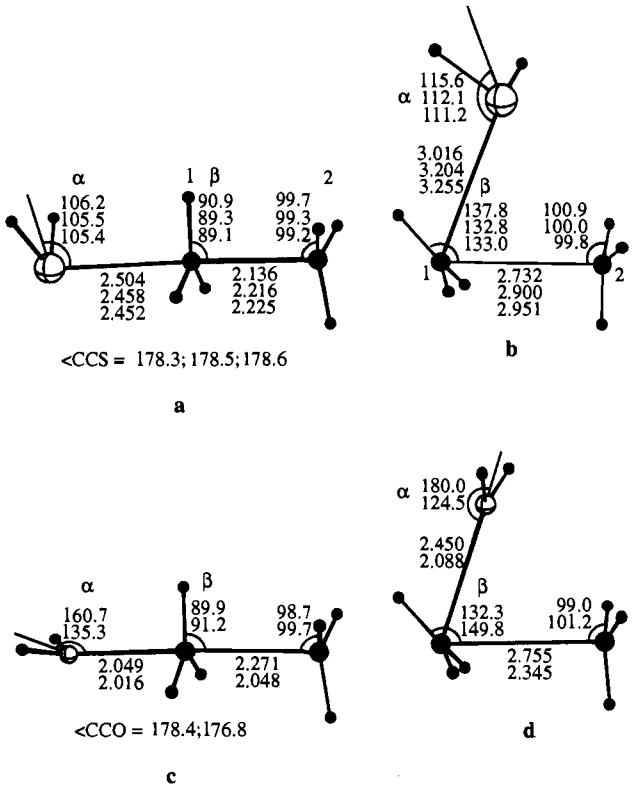

Figure 4. Optimized backside and frontside TS structures for $H_2S + C_2H_6^{\bullet+}$ (in a and b) and $H_2O + C_2H_6^{\bullet+}$ (in c and d). In (a) and (b) each geometric parameter has three values which correspond, respectively from top to bottom, to UHF/6-31G*, SCRF/UHF/6-31G* (CH_2Cl_2), and SCRF/UHF/6-31G* (CH_3CN). In (c) and (d) each geometric parameter has two values which correspond, respectively, from top to bottom, to HF/6-31G* and to UMP2/6-31G*. The nucleophile is drawn in each case by a hollow ball. C1 is the site of attack; C2 is the leaving group.

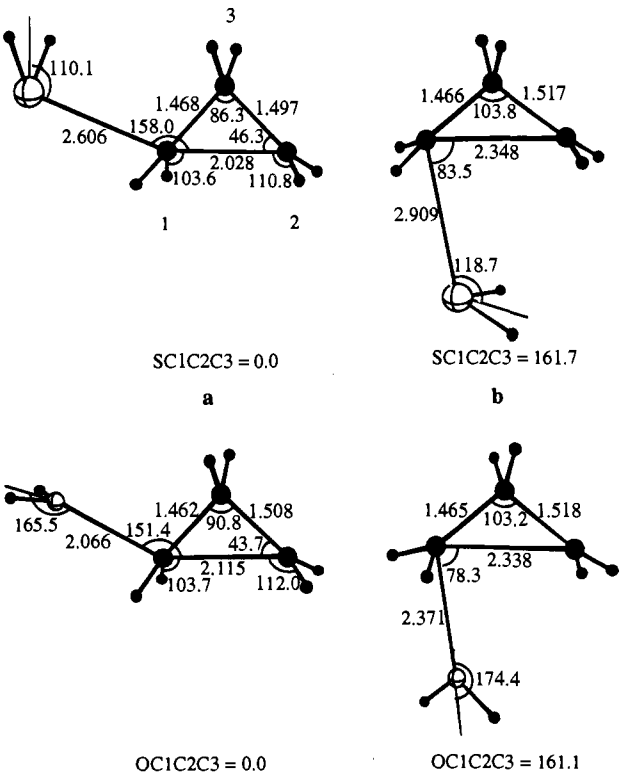

Figure 5. UHF/6-31G* optimized backside and frontside TS structures for $H_2S + C_3H_6^{\bullet+}$ (a and b) and for $H_2O + C_2H_6^{\bullet+}$ (for c and d). C1 is the site of attack, C2 is the leaving group, and C3 is the central carbon of the three-membered ring.

The same conclusions apply to the corresponding frontside TSs, and they also recur in the TSs for the $C_3H_6^{\bullet+}$ system. The differences exhibited by the H_2O and H_2S TSs suggest the existence *of two electronic categories that possess distinct TS bonding patterns and electronic structures*. We will return later to discuss these differences in more detail.

The reactions of NH_3 and PH_3 with $C_2H_6^{\bullet+}$ and NH_3 with $C_3H_6^{\bullet+}$, and the reaction of H_2S with $Si_2H_6^{\bullet+}$ (see Tables 1 and 2, entries 4–6; Table 3, entries 5 and 6), behave in an essential similar manner to the preceding cases. In all these combinations the backside trajectories proceed in a barrierless fashion,[36] while the frontside trajectories possess saddle point similar to ones discusses earlier.

B. Energies and Stereospecificity. We now turn to Tables 4 and 5 which collect the energetic features of the cleavage mechanisms following the notations of the energy quantities in the reaction profile in Figure 1.

Gas Phase Energetics. Entries 1a–d in Table 4 summarize the energy quantities for the reaction of H_2S with $C_2H_6^{\bullet+}$ (eq 1) at the various computational levels, including those in a preliminary study (entry 1c).[28] Firstly, it is seen that the stabilization energy, $E_R°$, of the backside reactant cluster is sensitive to the computational level and converges to 19–23 kcal/mol. In contrast, the stabilization energy of the frontside reactant cluster is rather insensitive to the level of computation and remains approximately 6–8 kcal/mol. Secondly, the stabilization energies of the product clusters are small, of the order of 3–5 kcal/mol, for either backside or frontside substitutions. This reflects the weak interaction of the charge species, $CH_3SH_2^+$, with the neutral $CH_3^{\bullet}$ in the C_P cluster. Third, the reaction energy values, ΔE_{RP}, especially at the correlated levels, are seen to be in good agreement with the value derived from experimental data.[37] Finally, the central barrier, $\Delta E_c^{\ddagger}$, for the backside mechanism persists on all levels and is small; approximately 0.5–2 kcal/mol, while the frontside barrier is approximately 26 kcal/mol.

Entries 2a–e in Table 4 summarize the energetics of the reaction of $C_2H_6^{\bullet+}$ with H_2O at both the UHF and the UMP2 levels of optimization. The stabilization energies of the backside and frontside reactant clusters, $E_R°$, is now much less sensitive to the level of calculation or optimization, reaching 18–20 kcal/mol. The stabilization energies of the product clusters, $E_P°$, are significantly larger for the frontside cluster. This last trend has its origins in the high positive charge on the protons of the H_2O moiety in the substitution product $CH_3OH_2^+$ that is stabilized by interacting with the negative charge on the carbon atom in the methyl radical. This interaction is absent in the backside cluster, and therefore the $E_P°$ value is similar to the H_2S case. The reaction energy converges to −25 kcal/mol,

(36) The backside trajectories of $H_3P/C_2H_6^{\bullet+}$, $H_2S/Si_2H_6^{\bullet+}$, and $H_3N/C_2H_6^{\bullet+}$ are barrierless. Starting however, from the frontside clusters, C_R of $H_2S/Si_2H_6^{\bullet+}$ and $H_3N/C_2H_6^{\bullet+}$ there exist saddle points which connect the frontside C_R clusters (Table 2) to the corresponding backside C_P clusters. The saddle points are conformational in nature; they do not involve electronic reorganization or geometrical reorganization of the principal bonds. The reaction vectors involve a swing motion of the nucleophiles from frontside to the backside position with frequencies as low as 33i/cm and 130i/cm. These conformational saddle points are not considered here.

(37) The reaction energy is given by

$$\Delta E_{RP} = D_{1e} - \text{MCA}$$

Here D_{1e} is the one-electron bond energy of the cation radical, and *MCA* is the methyl cation affinity or in the general case the alkyl (silyl) cation affinity. *MCA* values are taken from the Meot-Ner, M.; Karpas, Z.; Deakyne, C. A. *J. Am. Chem. Soc.* **1986**, *108*, 3913.

Table 1. Principal Structural Parameters[a,b] for the Critical Species in the Backside Nucleophilic Cleavage Mechanism for Nu/Cation Radical Pairs

entry	Nu/cation radical	species	$\langle S^2\rangle$[c]	d	r	α	β	γ	θ
1a	$H_2S/C_2H_6^{\bullet+}$	C_R	0.766	2.752	1.965	108.6	96.1	100.0	178.1
1b		TS	0.773	2.504	2.136	106.2	90.9	99.4	178.3
1c		C_P	0.760	1.835	3.460	113.0	72.1	95.9	177.8
1d		P	0.761	1.832	∞	106.6	69.8		
2a	$H_2O/C_2H_6^{\bullet+}$	C_R	0.758	2.410	2.006	180.0	96.7	99.0	179.3
2b		TS	0.758	2.049	2.271	160.7	89.9	98.7	178.4
2c		C_P	0.760	1.520	3.289	141.0	74.1	96.1	178.4
2d		P	0.761	1.511	∞	141.3	72.3		
3a	$(H_2O/C_2H_6^{\bullet+})$[d]	C_R	0.760	2.067	2.006	137.3	92.7	99.6	176.7
3b		TS	0.760	2.016	2.048	135.3	91.2	99.4	176.8
3c		C_P	0.760	1.530	3.116	133.2	74.0	95.9	177.8
3d		P	0.762	1.518	∞	133.7	71.5		
4a	$NH_3/C_2H_6^{\bullet+}$	C_R[g]							
4b		TS[g]							
4c		C_P	0.760	1.509	3.483	128.4	72.1	96.5	179.6
4d		P	0.761	1.506	∞	128.3	71.9		
5a	$PH_3/C_2H_6^{\bullet+}$	C_R[g]							
5b		TS[g]							
5c		C_P	0.760	1.811	3.617	128.6	70.0	96.3	179.6
5d		P	0.761	1.812	∞	128.5	70.5		
6a	$H_2S/Si_2H_6^{\bullet+}$	C_R[g]							
6b		TS[g]							
6c		C_P	0.754	2.364	3.500	108.3	81.3	104.4	177.6
6d		P	0.754	2.316	∞	108.0	76.2	–	–
7a	$H_2S/C_2H_6^{\bullet+}$, $\epsilon = 9.8$[e,f]	C_R	0.761	2.752	1.965	108.6	96.1	100.0	178.1
7b		TS	0.769	2.458	2.216	105.5	89.3	99.0	178.5
7c		C_R'	0.758	3.500	1.965	109.3	98.5	98.3	178.1
8a	$H_2S/C_2H_6^{\bullet+}$, $\epsilon = 35.9$[e]	C_R	0.761	2.752	1.965	108.6	96.1	100.0	178.1
8b		TS	0.769	2.452	2.225	105.4	89.1	99.0	178.6

[a] Unless noted otherwise the parameters are optimized by UHF/6-31G*. Bond lengths are in Å and angles in deg. [b] The labels of the parameters correspond to Figure 3. The critical species refer to Figure 1. [c] These are expectation values of S^2 operator. [d] These entries refer to UMP2/6-31G* optimization. [e] These entries refer to (SCRF/UHF)/6-31G* optimization. The ϵ values refer to dielectric constants. [f] C_R' is an encounter complex. C_R is the cluster with the gas phase geometry. [g] These backside trajectories are barrierless. Consult ref 36.

Table 2. Principal Structural Parameters[a,b] for the Critical Species in the Frontside Nucleophilic Cleavage Mechanism for Nu/Cation Radical Pairs

entry	Nu/cation radical	species	$\langle S^2\rangle$[d]	d	r	α	β (β')	γ (γ)	θ
1a	$H_2S/C_2H_6^{\bullet+}$	C_R	0.758	3.897	1.970	128.4	96.8(98.8)	98.2(98.5)	75.2
1b		TS	0.761	3.016	2.732	115.6	132.7(74.1)	91.9(100.9)	71.8
1c		C_P	0.759	1.831	3.829	106.4	123.7(41.6)	87.1(117.7)	65.7
2a	$H_2O/C_2H_6^{\bullet+}$	C_R	0.758	3.146	1.967	163.3	96.2(99.0)	99.0(96.2)	71.8
2b		TS	0.760	2.450	2.755	180.0	132.3(73.5)	94.8(99.0)	72.0
2c		C_P	0.758	1.500	3.960	140.4	148.0(83.1)	88.7(116.1)	43.7
3a	$(H_2O/C_2H_6^{\bullet+})$[c]	C_R	0.759	3.057	1.905	163.6	94.4(100.1)	97.8(98.5)	72.1
3b		TS	0.764	2.088	2.345	124.5	149.8(77.3)	91.7(101.7)	70.9
3c		C_P	0.759	1.502	3.799	132.5	149.7(82.7)	88.1(117.2)	44.8
4a	$NH_3/C_2H_6^{\bullet+}$	C_R	0.759	3.196	1.950	121.0	92.5(100.2)	97.6(99.3)	87.2
4b		TS	0.764	2.497	2.571	137.0	109.8(63.7)	98.0(98.5)	72.7
4c		C_P	0.759	1.503	4.116	128.2	157.9(80.9)	87.7(117.4)	49.5
5a	$PH_3/C_2H_6^{\bullet+}$	C_R	0.758	4.012	1.964	147.5	95.8(99.2)	98.3(98.5)	81.5
5b		TS	0.768	3.071	2.601	136.3	131.0(76.7)	91.5(101.9)	73.1
5c		C_P	0.760	1.812	4.936	127.5	157.5(82.7)	82.7(116.0)	47.9
6a	$H_2S/Si_2H_6^{\bullet+}$	C_R	0.754	3.976	2.702	128.4	100.2(95.5)	97.4(101.6)	79.3
6b		TS	0.758	2.642	2.929	106.0	146.3(81.5)	96.0(104.9)	78.1
6c		C_P	0.754	2.303	5.245	107.6	151.1(75.6)	80.9(115.4)	52.0
7a	$H_2S/C_2H_6^{\bullet+}$, $\epsilon = 9.8$[e,f]	C_R							
7b		TS	0.759	3.204	2.900	112.1	132.8(72.4)	92.2(100.0)	70.3
8a	$H_2S/C_2H_6^{\bullet+}$, $\epsilon = 35.9$[e,f]	C_R							
8b		TS	0.759	3.255	2.951	111.2	133.0(72.0)	92.5(99.6)	69.9

[a] These are UHF/6-31G* optimized parameters unless noted otherwise. Bond lengths are in Å and angles in deg. [b] The labels of the parameters correspond to Figure 3. The critical species refer to Figure 1. [c] These entries refer to UMP2/6-31G* optimization. A small imaginary frequency (100 i/cm) in C_R is ignored. [d] These are expectation values of S^2 operator. [e] These entries refer to (SCRF/UHF)/6-31G* optimization. The ϵ values refer to dielectric constants. [f] C_R is the cluster with the gas phase geometry.

which is now somewhat overestimated relative to the experimentally derived value.[37] As with H_2S, the stereospecificity of the H_2O reaction overwhelmingly favors the backside attack by at least 23 kcal/mol. The trend persists whether the geometry optimization is carried out at the UHF level or is upgraded to the UMP2 level.

Entries 3–9 in Table 4 show the results for the remaining nucleophilic cleavage reactions of $C_2H_6^{\bullet+}$, $Si_2H_6^{\bullet+}$, and $C_3H_6^{\bullet+}$. The backside pathways are seen to be either barrierless or to involve small barriers. On the other hand, the frontside mechanisms involve substantial barriers reflecting once more the stereochemical preference of the nucleophilic cleavage.

The reaction of H_2O with $C_3H_6^{\bullet+}$ (entry 8) is implicated in the gas phase experiments during the loss of H_2O from the cation

Table 3. Principal Structural Parameters[a] for the Critical Species in the Nucleophilic Cleavages, Nu + $C_3H_6^{\bullet+}$ → $^+NuCH_2CH_2CH_2^\bullet$

entry	Nu[b]	species	$\langle S^2\rangle$[c]	*d*	*r*	δ	α	θ	<NuC$_1$C$_2$C$_3$
1a	H_2S(B)	C_R	0.778	3.135	1.894	79.8	122.6	151.6	0.0
1b		TS	0.775	2.626	2.028	86.3	110.1	158.0	0.0
1c		P	0.763	1.859	2.477	109.4	106.3	148.9	0.0
2a	H_2S(F)	C_R	0.780	3.706	1.869	78.6	166.3	76.7	180.0
2b		TS	0.769	2.909	2.348	103.8	118.7	83.5	161.7
2c		P	0.761	1.853	2.538	113.7	105.6	96.5	125.0
3a	H_2O(B)	C_R	0.776	2.440	1.917	81.0	173.5	154.3	0.0
3b		TS	0.769	2.066	2.115	90.8	165.5	151.4	0.0
3c		P	0.763	1.556	2.450	108.4	140.0	146.5	0.0
4a	H_2O(F)	C_R	0.780	2.963	1.860	78.1	161.7	71.8	180.0
4b		TS	0.768	2.371	2.338	103.2	174.4	78.3	161.1
4c		P	0.761	1.540	2.509	112.6	136.0	90.2	126.5
5a	NH_3(B)	C_R							
5b		TS							
5c		P	0.763	1.520	2.494	110.7	127.9	144.7	0.0
6a	NH_3(F)	C_R	0.779	3.073	1.852	77.8	115.1	72.5	178.8
6b		TS	0.775	2.492	2.212	96.2	135.4	78.5	180.0
6c		P	0.761	1.517	2.524	112.9	128.9	92.0	124.5

[c] UHF/6-31G* optimized parameters. Bond lengths are in Å and angles in deg. [b] (B) and (F) correspond to backside and frontside, respectively. [c] These are expectation values of S^2 operator.

Table 4. Computed Energies[a] for the Reaction of Nu: with $RH^{\bullet+}$

entry	Nu/cation radical	computational level[b]	$E_R°$ (B, F)	$E_P°$ (B, F)	ΔE_{RP}	$\Delta E_C^‡$ (B, F)
1a	$H_2S/C_2H_6^{\bullet+}$	UHF/6-31G*//6-31G*	−8.5, −6.3	−2.0, −3.8	−26.5	0.51, 24.6
1b		MP2/6-31G*//6-31G*	−18.8; −7.9	−2.7; −5.2	−35.0	0.16; 26.9
1c		CISD(FC)+corr/3-21G*(d)//3-21G*(d)	−21.1; −7.6		−32.9	1.90; 22.9
1d		QCISD(T)/6-31G*//6-31G*	−22.9; −7.6	−2.7; −5.1	−33.9(−35±2)[b]	1.96; 25.7
2a	$H_2O/C_2H_6^{\bullet+}$	UHF/6-31G*//6-31G*	−14.7; −14.5	−2.9; −8.9	−23.0	1.5; 24.0
2b		MP2(FC)/6-31G*//6-31G*	−17.7; −16.7	−3.7; −12.0	−26.2	0.8; 29.8
2c		QCISD(T)(FC)/6-31G*//6-31G*	−17.9; −16.5	−3.7; −11.7	−25.4	0.3; 26.5
2d		UMP2(FC)/6-31G*//UMP2(FC)/6-31G*	−18.9; −16.9	−3.9; −12.5	−26.1	0.06; 25.9
2e		QCISD(T)(FC)/6-31G*//UMP2(FC)/6-31G*	−19.5; −16.7	−3.9; −12.1	−25.3(−19±3)[b]	0.0; 23.3
3	$NH_3/C_2H_6^{\bullet+}$	UHF/6-31G*//6-31G*	−15.0; −15.0	−2.1; −5.8	−61.2(−56.2±2)[b]	1.6;[c] 20.0
4	$PH_3/C_2H_6^{\bullet+}$	UHF/6-31G*//6-31G*	−6.6; −6.6	−1.6; −3.0	−53.9	<0; 19.6
5a	$HF/C_2H_6^{\bullet+}$	UHF/3-21G*(d)//3-21G*(d)	−13.6; −15.3	−13.6	−2.8(−4±2)[b]	<0; 26.4
5b	$HF/C_2H_6^{\bullet+}$	MP2(FC)/3-21G*(d)//3-21G*(d)	−17.5	−17.5	−7.3	<0; 29.8
6	$H_2S/Si_2H_6^+$	UHF/6-31G*//6-31G*	−5.1; −5.1	−2.7; −2.1	−13.5	<0; 9.9
7	$H_2S/C_3H_6^{\bullet+}$	UHF/6-31G*//6-31G*	−5.1; −5.5		−19.6; −20.6	1.3; 14.8
8	$H_2O/C_3H_6^{\bullet+}$	UHF/6-31G*//6-31G*	−13.5; −12.4		−19.5; −21.1	1.1; 12.4
9	$NH_3/C_3H_6^{\bullet+}$	UHF/6-31G*//6-31G*	−; −13.1		−54.3; −56.0	<0; 8.2

[a] The quantities refer to Figure 1. All values are in kcal/mol. B refers to backside and F refers to frontside. [b] Experimental values are in parentheses. See ref 37.

Table 5. Central Barriers[a] for the Backside and Frontside Nucleophilic Cleavage Reactions of H_2S and $C_2H_6^{\bullet+}$ in the Gas Phase and in Two Solvents

dielectric constant (solvent)	$\Delta E_C^‡$ (B)	$\Delta E_C^‡$ (F)
1.0 (gas phase)	0.51	24.6
9.08 (CH_2Cl_2)	2.44	25.8
9.08 (CH_2Cl_2)	5.60[b]	
35.9 (CH_3CN)	2.83	25.9
35.9 (CH_3CN)	6.20[b]	

[a] All values are in kcal/mol. Barriers in a solvent are relative to the cluster at its gas phase geometry. [b] This barrier is relative to an encounter complex.

radical of propanol and other analogs.[38] The computed stabilization energies of the $H_2O/C_3H_6^{\bullet+}$ clusters are close to the experimentally estimated values,[38a] and the presence of a nucleophilic substitution barrier is in qualitative accord with the energy profile deduced by Bowen et al.[38a] from experimental results and thermochemical data. Our central barrier data indicates that both backside as well as frontside mechanisms are feasible under the conditions of the gas phase experiment.

The reactions of HF with $C_2H_6^{\bullet+}$ (entry 5, Table 4)[39a] were included in order to study the stereoselection at the limit of poor nucleophilicity. As can be seen, the cation radical is cleaved very easily from the backside but has a substantial barrier for a frontside cleavage. Essentially similar results were obtained for the reaction of HF with $C_3H_6^{\bullet+}$.[39b] However, since the data are incomplete,[39] this reaction is not included in Table 4. The small barrier for the backside reaction indicates that the $C_2H_6^{\bullet+}$ and $C_3H_6^{\bullet+}$ cation radicals are likely to undergo a facile nucleophilic-assisted backside bond cleavage even in fluorinated matrices. There are obvious implications on the discussion of the structure of the $C_3H_6^{\bullet+}$ species in these matrices.[40]

Solution Phase Energetics. In order to ascertain the stereospecificity in solution, we display in Table 5 the SCRF data for the reaction of H_2S with $C_2H_6^{\bullet+}$ in two solvents with dielectric constants corresponding to CH_2Cl_2 and CH_3CN. Since no clusters could be located on the SCRF energy surface, the barriers in solution were evaluated relative to the reactant

(38) (a) Bowen, R. D.; Colburn, A. W.; Derrick, P. J. *J. Am. Chem. Soc.* **1991**, *113*, 1132. (b) Audier, H. E.; Milliet, A.; Sozzi, G., Hammerum, S. *Adv. Mass Spectrom.* **1989**, *11*, 922. (c) Shao, J.-D.; Baer, T.; Morrow, J. C.; Fraser-Monteiro, M. L. *J. Chem. Phys.* **1987**, *87*, 5242. (d) For other reactions of $C_3H_6^{\bullet+}$ and a general discussion of its reactivity, *inter alia*, see: Stirk, K. M.; Kiminkinen, L. K. M.; Kenttamaa, H. I. *Chem. Rev.* **1992**, *92*, 1649.

(39) (a) Cho, J. K.; Shaik, S. 3-21G* and 3-21G*(d) studies (see also ref 28) of HF/$RH^{\bullet+}$ combinations. (b) An exploration of the $C_3H_6^{\bullet+}$ ring opening by HF, by means of 3-21G* calculations, resulted in a barrierless process.

(40) (a) Qin, X.-Z.; Williams, F. *Tetrahedron* **1986**, *42*, 6301. (b) Symon, M. C. R. *Chem. Phys. Lett.* **1985**, *117*, 383. (c) For a related discussion see ref 24a.

Table 6. Computed Group Spin (ϱ) Density and Charge (Q) Distributions in the TSs [(Nu···G_1···G_2)$^{\bullet+}$][a] of Nucleophilic Cleavage Reactions

			ϱ, Q(B)			ϱ, Q(F)		
entry	Nu/RH$^{\bullet+}$	computational level	Nu	G_1	G_2	Nu	G_1	G_2
1a	$H_2S/C_2H_6^{\bullet+}$	PUHF//UHF	0.134, 0.291	0.185, 0.430	0.681, 0.279	0.021, 0.095	0.106, 0.782	0.873, 0.123
1b		PUMP2(FC)//UHF	0.231, 0.395	0.163, 0.293	0.606, 0.312	0.049, 0.146	0.200, 0.619	0.751, 0.235
1c		PQCISD(T)(FC)//UHF	0.142, 0.324	0.199, 0.384	0.659, 0.292	0.021, 0.117	0.141, 0.726	0.838, 0.157
1d		PQCISD(T)//UHF	0.140, 0.321	0.201, 0.386	0.659, 0.293			
1e		SCRF/PUHF//UHF						
		$\epsilon = 9.08$	0.108, 0.294	0.169, 0.452	0.723, 0.254	0.010, 0.057	0.066, 0.867	0.924, 0.076
		$\epsilon = 35.9$	0.106, 0.296	0.167, 0.453	0.727, 0.251	0.008, 0.051	0.058, 0.883	0.934, 0.066
2a	$H_2O/C_2H_6^{\bullet+}$	PUHF//UHF	0.020, 0.117	0.205, 0.659	0.775, 0.224	0.006, 0.054	0.101, 0.846	0.893, 0.100
2b		PUMP2(FC)//UHF	0.040, 0.163	0.250, 0.553	0.710, 0.284	0.013, 0.077	0.202, 0.722	0.785, 0.201
2c		PQCISD(T)(FC)//UHF	0.018, 0.142	0.228, 0.614	0.754, 0.244	0.005, 0.069	0.133, 0.802	0.862, 0.129
2d		PUMP2(FC)//UMP2	0.078, 0.201	0.278, 0.472	0.644, 0.327			
2e		PQCISD(T)(FC)//UMP2	0.044, 0.167	0.280, 0.529	0.676, 0.304			
3	$NH_3/C_2H_6^{\bullet+}$	UHF//UHF				0.050, 0.110	0.120, 0.640	0.830, 0.150
4	$PH_3/C_2H_6^{\bullet+}$	UHF//UHF				0.070, 0.140	0.090, 0.710	0.840, 0.150
5	$H_2S/Si_2H_6^{\bullet+}$	UHF//UHF				0.060, 0.250	0.300, 0.420	0.630, 0.330
6	$H_2S/C_3H_6^{\bullet+}$	UHF//UHF	0.070, 0.190	0.250, 0.390	0.810, 0.230	0.040, 0.110	0.050, 0.600	1.00, 0.160
					(−0.122, 0.200)[b]			(−0.090, 0.120)[b]
7	$H_2O/C_3H_6^{\bullet+}$	UHF//UHF	0.015, 0.108	0.200, 0.538	0.907, 0.172	0.009, 0.056	0.092, 0.660	0.998, 0.173
					(−0.122, 0.181)[b]			(−0.099, 0.111)[b]
8	$NH_3/C_3H_6^{\bullet+}$	UHF//UHF				0.040, 0.100	0.130, 0.590	0.930, 0.180
								(−0.100, 0.130)[b]

[a] G_1 and G_2 are groups of the cation radical. G_1 is the site of attack and G_2 is the leaving group. [b] These values correspond to the central CH_2 group of $C_3H_6^{\bullet+}$.

clusters located for the gas phase reaction. In the backside cleavage of $C_2H_6^{\bullet+}$ by H_2S, the barriers were also estimated relative to an encounter complex. The encounter complex was modeled by optimizing the structure at fixed S−C_1 and C_1−C_2 distances of 3.5 and 1.965 Å, respectively. The fixed S−C_1 distance is the sum of the corresponding van der Waals radii, and the fixed C_1−C_2 distance corresponds to the bond length of the cation radical in the gas phase cluster.

The barriers in a solvent are seen to be higher than the corresponding central barriers in the gas phase. This trend originates in the larger dipole of the encounter complex or cluster relative to the TS. The barriers also increase, albeit modestly, with the polarity of the solvent in accord with the experimental findings in related systems.[41] Most importantly, *the solvent does not change the stereospecificity of the cleavage reaction which still strongly favors a backside nucleophilic attack.*

C. Charge and Spin Density Distribution. The charge (Q) and spin (ϱ) distributions provide important mechanistic insight[21] into the electronic features of the nucleophilic cleavage reactions.

Electronic Structures of TSs. Table 6 summarizes spin and charge density data for representative backside and frontside TS structures. Entries 1 and 2 show data for the TSs of $H_2S/C_2H_6^{+\bullet}$ and $H_2O/C_2H_6^{+\bullet}$ at different computational levels. Generally speaking, the MP2 wave function places a significant spin density on the nucleophile, Nu. This is apparent especially in the $H_2S/C_2H_6^{\bullet+}$ TS in entry 1b vs 1a but is also evident in the $H_2O/C_2H_6^{\bullet+}$ TS in entry 2b vs 2a. Upgrading the projected wave function to the QCISD(T) level decreases in each case the nucleophile's spin density and restores approximately the PUHF results (e.g., entries 1c and 1a). It is apparent, therefore, that the UMP2 wave function exaggerates the importance of an electron-transferred configuration which places unpaired spin density on Nu, while QCISD(T) as well as UHF reduce the weight of this configuration. Accepting the higher quality of the QCISD(T) wave function, we rely henceforth on the QCISD(T) results or on the UHF results whenever QCISD(T) data were not available.

Looking at these data we note the following trends.

(i) There is a disparity between the positive charge and the free spin density located on each moiety of the TS. This disparity has a mechanistic significance. For example, the disparity on the nucleophile (Nu) means that this group has a character of a Nu$^{\bullet+}$ species where part of the spin is paired up, but part of it remains free. Since the Nu group starts as a neutral Nu:, this indicates an electron transfer character in the substitution TS.

(ii) In all of the TSs, the site of nucleophilic attack (group G_1 of the cation radical moiety) possesses the highest positive charge, while the leaving group moiety (G_2) possesses the highest spin density. This indicates a major involvement of a VB configuration of the type, Nu: G_1^+ $G_2^{\bullet}$.

(iii) Inspection of entry 1c shows that the frontside TS for $H_2S/C_2H_6^{\bullet+}$ has a more localized nature in comparison with its backside isomer, having 84% of the total spin on the G_2 group of the cation radical moiety, while the G_1 group bears 73% of the positive charge. This trend is apparent, albeit more subtly, in all other cases of backside vs frontside TSs. Since spin and charge delocalization is a sign of good overlap bonding between the Nu and the cation radical moiety, it follows that the frontside TS is significantly less bonded in comparison with the backside TS. This conclusion is in agreement with the overlap population and geometric data of the respective TSs and is a strong implication of orbital symmetry constraints which prevent good bonding in the frontside TS.

(iv) The nature of the TS is seen to depend on the nature of the nucleophile. This is more apparent in the backside structures and particularly in the H_2S vs H_2O cases (entries 1c vs 2c). Thus, the $H_2S/C_2H_6^{\bullet+}$ TS exhibits significant spin density delocalization, in contrast with the H_2O TS where 98% of the spin density resides on the original cation radical moiety and mostly on the G_2 group. Similar but somewhat attenuated trends are exhibited by the backside TSs of H_2O vs H_2S in the $C_3H_6^{\bullet+}$ case (entries 6 and 7); the former being more localized than the latter. There seem to exist then two classes that differ in the electronic structures of the TSs. This conclusion is commensurate with the overlap population and structural data discussed above.

Electronic Structure of the Product States. Table 7 displays the charge distribution patterns of the product state for

(41) Dinnocenzo, J. P.; Farid, S.; Goodmann, J. L.; Gould, I. R.; Todd, W. P. *Mol. Cryst. Liq. Cryst.* **1991**, *194*, 151.

Table 7. Computed Group Charges (Q) in the Products of Nucleophilic Cleavage, $(NuG_1)^+/G_2^\bullet$

entry	$(Nu-G_1)^+/G_2^\bullet$	computational level	Q (Nu)	Q (G_1)	Q (G_2)
1a	$(H_2S-CH_3)^+/CH_3^\bullet$	UHF//UHF	0.810	0.190	0.000
1b		QCISD(T)//UHF	0.811	0.189	0.000
2a	$(H_2O-CH_3)^+/CH_3^\bullet$	UHF/UHF	0.400	0.600	0.000
2b		QCISD(T)//UHF	0.441	0.559	0.000
3a	$(NH_3-CH_3)^+/CH_3^\bullet$	UHF//UHF	0.570	0.430	0.000
3b		QCISD(T)//UHF	0.596	0.404	0.000
4a	$(PH_3-CH_3)^+/CH_3^\bullet$	UHF//UHF	0.930	0.070	0.000
4b		QCISD(T)//UHF	0.908	0.092	0.000
5	$(H_2S-SiH_3)^+/SiH_3^\bullet$	UHF//UHF	0.380	0.620	0.000
6	$(H_2S-CH_2CH_2CH_2^\bullet)^+$	UHF//UHF[a]	0.770	0.050	0.110
7	$(H_3N-CH_2CH_2CH_2^\bullet)^+$	UHF//UHF[a]	0.540	0.310	0.100
8	$(H_2O-CH_2CH_2CH_2^\bullet)^+$	UHF//UHF[a]	0.345	0.492	0.109

[a] The charge on the central CH_2 group is not indicated. G_2 is the terminal CH_2 group.

the different target reactions. Two distinct patterns are apparent, depending on the location of the largest positive charge on Nu or on G_1 in the substitution product, $(NuG_1)^+/G_2^\bullet$. Entries 1, 3, 4, 6, and 7, where the nucleophiles are H_2S, NH_3, and PH_3, represent one pattern where the positive charge is localized mostly on the Nu moiety. The second pattern, represented by the case of H_2O as nucleophile (entries 2 and 8) as well as by $H_2S-SiH_3^+/SiH_3^\bullet$ (entry 5), localizes the positive charge more on the G_1 group. These two patterns correspond to the type observed in point (iv) above for the respective TS structures. Thus, there seem to exist two reaction classes which depend on the donor/acceptor properties of the Nu/cation-radical pair and which differ in the electronic structure of their TSs and product states.

Discussion

The computational results reveal a three-dimensional mechanistic problem. One dimension is the origin of the overwhelming stereospecificity in favor of the backside nucleophilic cleavage, be it in the gas phase or in a solution phase; a trend that is corroborated by experiment.[6] The second dimension is the electronic structure of the TS and its dependence on the stereochemistry as well as on the donor/acceptor nature of the Nu/cation-radical pair. An important aspect of this second dimension is the possible emergence of two classes of substitution reactions that differ in the electronic structures of their corresponding TSs. The third dimension of the problem is concerned with the reactivity patterns and especially with the very small barriers for the backside nucleophilic cleavage in either the gas phase or in solution phase. Small barriers are observed also in many of the experimental systems in the gas phase[11,38d] and in solution.[6,41]

The following section addresses these mechanistic aspects by a VB analysis and modeling of the charge and spin density data.[21]

A. VB Modeling of the Electronic Structure in Nucleophilic Cleavages of Cation Radicals. VB Configurations. Shown in **1**–**4** is a set of effective[42] VB configurations that are essential for the description of the reaction complex in the case of a nucleophile reacting with a simple σ-cation radical. The G_1 and G_2 symbolize the groups of the cation radical (e.g., G = CH_3).

The configurations **1** and **2** describe a neutral nucleophile with an electron pair and corresponding cation radical structures that place the charge and spin on the G_1 and G_2 groups. The

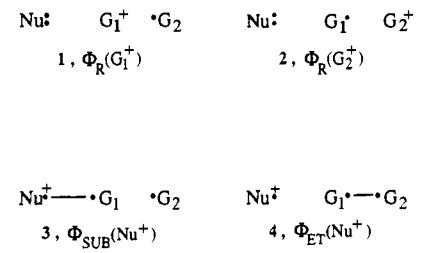

labels of these configurations as $\Phi_R(G_1^+)$ and $\Phi_R(G_2^+)$ signify their relation to the reactant state (R) as well as the location of the positive charge. Configuration **3** describes the Heitler–London (HL) spin-paired bond[42] between Nu and G_1, as indicated by the line connecting the two dots. This configuration is denoted as $\Phi_{SUB}(Nu^+)$ to signify its contribution to the bonding in the substitution product and the location of the positive charge on the Nu. Similarly, **4** describes the HL bond between G_1 and G_2 and is denoted as $\Phi_{ET}(Nu^+)$ to describe its origins by an electron transfer (ET) from the Nu: to the cation radical.

As shown in Appendix 1 the wave function constructed from a linear combination of **1**–**4** can predict the charge and spin densities of the TSs as well as of other critical points with remarkable accuracy (deviations of 0.001e or smaller). While we are not enamoured with this accuracy, it nevertheless indicates that the four VB configurations capture the qualitative essence of the electronic structure as revealed in Tables 6 and 7 above. Thus, the combination of $\Phi_{SUB}(Nu^+)$, **3**, and $\Phi_{ET}(Nu^+)$, **4**, will provide the disparity of charge and spin on the Nu moiety. Similarly, the combination of $\Phi_R(G_1^+)$, **1**, and $\Phi_R(G_2^+)$, **2**, will lead to the charge-spin disparity on the other moieties of the cation radical, while the larger contribution of $\Phi_R(G_1^+)$ to the wave function will account for the highest positive charge on the site of attack, G_1. For more complex cation radicals, e.g., $C_3H_6^{\bullet+}$, a quantitative analysis will require more configurations because of the need to account for charge and spin densities on G_3, the third group of the cation radical. Nevertheless, the configurations in **1**–**4** will still give a correct *qualitative* description also in these more complex situations.

VB Analysis along the Reaction Coordinate. The wave function, Ψ, along the reaction coordinate can be written in the common way as a linear combination[43] of the contributing VB structures, in eq 4. The coefficients of the four configurations follow from the group charges and spin densities of the reaction complex in eqs 4–6.

$$\Psi = \Sigma_i d_i \Phi_i \tag{3}$$

$$d_1[\Phi_R(G_1^+)] = [Q(G_1)]^{1/2} \tag{4}$$

$$d_2[\Phi_R(G_2^+)] = [Q(G_2)]^{1/2} \tag{5}$$

$$d_3[\Phi_{SUB}(Nu^+)] = [|Q(Nu) - \varrho(Nu)|]^{1/2} \tag{6}$$

$$d_4[\Phi_{ET}(Nu^+)] = [|1 - Q(G_2) - \varrho(G_2)|]^{1/2} \tag{7}$$

Table 8 collects the derived coefficients for $H_2S/C_2H_6^{\bullet+}$ and $H_2O/C_2H_6^{\bullet+}$ in the two stereochemical pathways. These reactions were chosen because they represent the two electronic categories discussed above and are called hereafter *class A and class B*, respectively. The table shows that the dominant configurations throughout the reaction profile are the reactant configurations $\Phi_R(G_1^+)$ and $\Phi_R(G_2^+)$, and the substitution configuration $\Phi_{SUB}(Nu^+)$, *and that* $\Phi_{SUB}(Nu^+)$ *replaces* $\Phi_R(G_2^+)$ *along the reaction coordinate.* Furthermore the TSs and especially in *Class A* are seen to involve some electron transfer character, $\Phi_{ET}(Nu^+)$.

(42) Shaik, S. S. In *New Theoretical Concepts for Understanding Organic Reactions*; Bertran, J., Csizmadia, I. G., Eds.; Kluwer Academic Publishers: Dordrecht, 1989; NATO ASI Series, Vol. C267, pp 165–218.

Table 8. Coefficients of the VB Configurations along the Reaction Coordinate for $H_2S/C_2H_6^{\bullet+}$ and $H_2O/C_2H_6^{\bullet+}$

		$d_i(B, B)^{a,b}$				
Nu/*Class*	coefficient (VB structure)	R	C_R	TS	C_P	P
H_2S/*A*	d_1 (**1**)	0.71, 0.71	0.63, 0.70	0.62, 0.85	0.44, 0.43	0.43, 0.43
	d_2 (**2**)	0.71, 0.71	0.62, 0.70	0.54, 0.40	0.10, 0.16	0.00, 0.00
	d_3 (**3**)	0.00, 0.00	0.28, 0.14	0.43, 0.31	0.89, 0.88	0.90, 0.90
	d_4 (**4**)	0.00, 0.00	0.27, 0.04	0.22, 0.07	0.04i,[c] 0.04i[c]	0.00, 0.00
H_2O/*B*	d_1 (**1**)	0.71, 0.71	0.73, 0.69	0.78, 0.90	0.75, 0.74	0.75, 0.75
	d_2 (**2**)	0.71, 0.71	0.64, 0.69	0.49, 0.36	0.13, 0.28	0.00, 0.00
	d_3 (**3**)	0.00, 0.00	0.21, 0.20	0.35, 0.25	0.65, 0.54	0.66, 0.66
	d_4 (**4**)	0.00, 0.00	0.08, 0.13	0.05, 0.09	0.03i;[c] 0.11	0.00, 0.00

[a] The coefficients are obtained from eqs 4–7 using PQCISD(T) charges and spin densities from Table 6. [b] The critical species refer to Figure 1. [c] These values are imaginary because the term under square root in eq 7 is negative. Actually the values are small and may reflect rounding off errors. For all practical purposes these values may be taken as ~0.

VB Configuration Crossing and the Mechanistic Classes of Nucleophilic Cleavage Reactions. The variation in the coefficients of the three principal configurations can be translated pictorially to the VB curve crossing diagrams shown in Figure 6a,b for *classes A* and *B*, respectively. The configurations are drawn from reactant to product clusters, both to restrict the discussion to the VB mixing aspects and to avoid an explicit consideration of electrostatic factors that stabilize the clusters. The final reaction profile that arises from the VB mixing is drawn in Figure 6 in bold lines. The relative contributions of the various electronic structures to the clusters and the TSs can be read from the coefficient data in Table 8.

Figure 6a,b simply mirror the variations of the VB coefficients in Table 8. Nonetheless, a brief explanation of the behavior of the individual configurations is warranted at this point. The rise of $\Phi_R(G_2^+)$ along the reaction coordinate is due to the build-up of a repulsive three-electron interaction[42] between the Nu: and $G_1^\bullet$ fragments (see **2**). A repulsive interaction exists also in $\Phi_{SUB}(Nu^+)$ because the two odd electrons in the $G_1^\bullet$–G_2 moiety (see **3**) possess *a major triplet character*.[42,44] Consequently, $\Phi_{SUB}(Nu^+)$ starts high in energy at the reactant stage and is stabilized along the reaction coordinate due to the release of the repulsive $G_1^\bullet$–G_2 interaction and due to creation of the $Nu^\bullet - {}^\bullet G_1$ HL bond. In contrast, the $\Phi_R(G_1^+)$ curve is relatively flat because it primarily involves interchange of electrostatic interactions of the charged fragment, G_1^+, with the neutral fragments $G_2^\bullet$ and Nu:, and this roughly balances out along the reaction coordinate.

We next turn to discuss the VB mixing aspects of Figure 6a,b. Initially at the reactant extreme, $\Phi_R(G_2^+)$ and $\Phi_R(G_1^+)$, which are degenerate, mix and form the reactant state in eq 8.

$$\Psi = \Psi_R = (2)^{-1/2}[\Phi_R(G_1^+) + \Phi_R(G_2^+)] \qquad (8)$$

This mixing of $\Phi_R(G_1^+)$ and $\Phi_R(G_2^+)$ is responsible for bonding between the G_1 and G_2 fragments of the cation radical, and the strength of the interaction determines the bond energy of the cation radical. Along the reaction coordinate, the mixing of $\Phi_R(G_1^+)$ and $\Phi_R(G_2^+)$ is gradually turned off. Consequently, the coefficient of $\Phi_R(G_2^+)$ at the ground state's wave function decreases and finally diminishes to zero at the product stage. While this is happening, $\Phi_{SUB}(Nu^+)$—which is initially an excited configuration—begins to mix in with $\Phi_R(G_1^+)$, and the mixing coefficient increases to its maximum value at the product extreme.

At the product extreme, $\Phi_{SUB}(Nu^+)$ and $\Phi_R(G_1^+)$ mix and thereby generate the product state with the wave function in eq 9. This mixing accounts for the electron pair bonding between Nu and G_1.

$$\Psi = \Psi_P = d_1\Phi_R(G_1^+) + d_3\Phi_{SUB}(Nu^+) \qquad (9)$$

$$d_1 = [Q(G_1)]^{1/2}, \quad d_3 = [Q(Nu)]^{1/2}$$

It is here at the product stage that we encounter the basis for the different electronic classifications *A* and *B*. In *class A*, $\Phi_{SUB}(Nu^+)$ is the lowest configuration (Figure 6a), and the $(Nu-G_1)^+$ bond possesses a major HL character and a charge distribution pattern typified by Q (Nu) > Q (G_1), as shown above in Table 7. In *class B*, $\Phi_{SUB}(Nu^+)$ remains above $\Phi_R(G_1^+)$ throughout the reaction profile (Figure 6b), and consequently the $(Nu-G_1)^+$ bond is dominated by the Nu: G_1^+ form and has the charge distribution pattern Q (G_1) > Q (Nu).[45] Thus, in *class A* the $(Nu-G_1)^+$ bond is "covalent-type", while in *class B* the same bond is "dative-type", similar to the dative bonds between ligand and positive metallic centers.

The behavior of $\Phi_R(G_1^+)$, **1**, and $\Phi_{SUB}(Nu^+)$, **3**, depends on their initial vertical energy gaps at the reactant stage in Figure 6. This vertical gap is composed of the electron transfer energy from the Nu: to the cation radical moiety as well as from the resulting triplet repulsion in the $G_1^\bullet$–G_2 moiety.[15,44] For a given cation radical, the vertical gap depends only on the donor/acceptor relationship of the two reactants. Thus in *class A* (Figure 6a), which is represented by H_2S with a low ionization potential, the vertical gap is small and consequently $\Phi_{SUB}(Nu^+)$ crosses below $\Phi_R(G_1^+)$. On the other hand, in *class B* which is represented by the nucleophile H_2O which possesses a high ionization potential, the vertical gap is large, and $\Phi_{SUB}(Nu^+)$ remains above $\Phi_R(G_1^+)$ throughout the reaction coordinate. Thus, the two electronic classes differ by the presence or absence of VB crossing of the principal structures of reactants and products, $\Phi_R(G_1^+)$ *and* $\Phi_{SUB}(Nu^+)$. As shall be seen below, this feature influences the electronic structures of the TSs for the two reaction types.

B. The Mechanism of TS Formation in the Gas Phase and in Solution. Inspection of the VB coefficients in the column entitled TS in Table 8 reveals that the coefficients of $\Phi_R(G_2^+)$ and $\Phi_{SUB}(Nu^+)$ are fairly close. This information is shown on the reaction coordinate in Figure 6a,b which indicate that the TS is located near the crossing geometry (C) of $\Phi_R(G_2^+)$ and $\Phi_{SUB}(Nu^+)$, slightly on the early side where $\Phi_R(G_2^+)$ is still lower in energy.

The location of the TS near point C can be rationalized by considering the major configuration mixings along the reaction

(43) The sum $\sum_i d_i^2$ in eq 8 is not unity because Φ_{SUB} and Φ_{ET} share a common determinant. For normalization constants of VB wave functions see the Appendix of ref 42 and the Appendix in the following: Shaik, S. S.; Duzy, E.; Bartuv, A. *J. Phys. Chem.* **1990**, *94*, 6574.

(44) In the wave function of Φ_{SUB}, $Nu^{\bullet+}$ and $^\bullet G_1$ are paired to a singlet, while the spin situation of $G_1^\bullet$ and $G_2^\bullet$ is 75% triplet. For discussion of such a three-electron wave function, see: Shaik, S.; Hiberty, P. C.; Lefour, J. M.; Ohanessian, G. *J. Am. Chem. Soc.* **1987**, *109*, 363 (especially Appendix 1).

(45) Goldstein, S.; Czapski, G.; Cohen, D.; Meyerstein, D.; Shaik, S. *J. Chem. Soc., Faraday Trans.* **1993**, *89*, 4045.

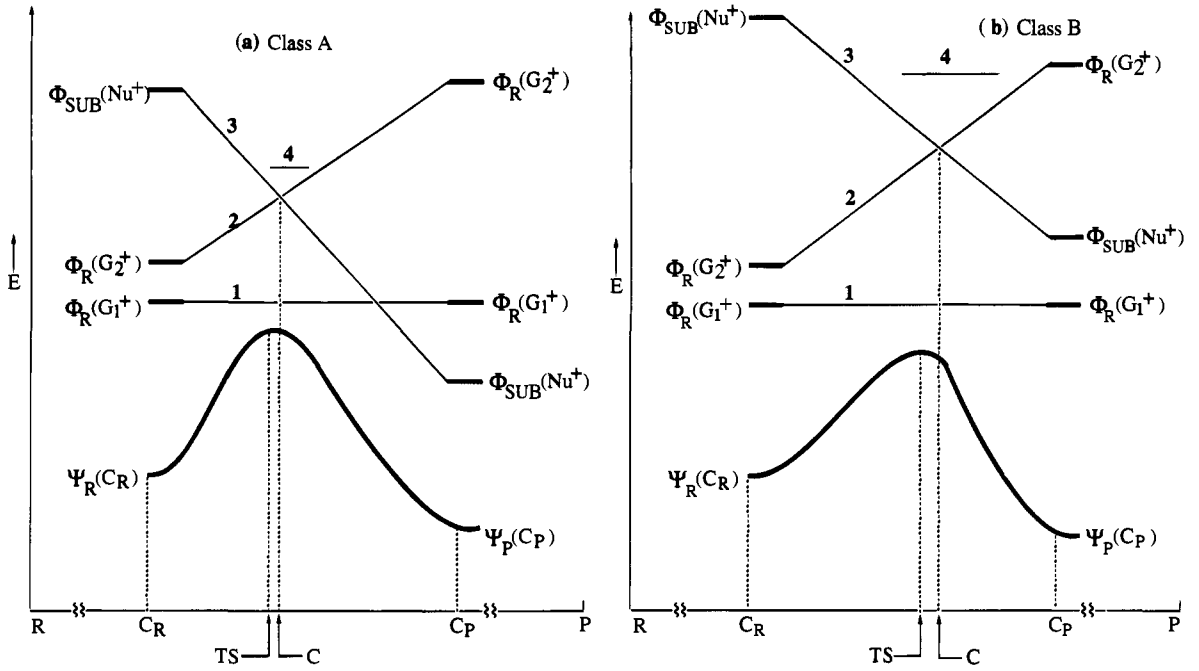

Figure 6. Schematic energy variation of the VB configurations **1**–**4** along the reaction coordinate, based on the VB data in Table 8. The energy level of **4** is shown only at the vicinity of the crossing geometry (C). The final profile resulting from the mixing of these VB configurations is shown by a thicker line: (a) The VB crossing situation in *class A* where the nucleophile possesses a low ionization potential. (b) The VB crossing situation in *class B* where the nucleophile has a high ionization potential. Note that in (b) $\Phi_R(G_1^+)$ is the ground configuration throughout the reaction profile. For convenience, the VB configurations and their mixing is limited to the reaction coordinate range between the clusters, C_R and C_P.

Table 9. VB Coefficients in the $(H_2S{\cdots}CH_3{\cdots}CH_3)^+$ TS in the Gas Phase and in Two Solvents[a]

configuration	coefficient	gas phase (B; F)	CH_2Cl_2 (B, F)	CH_3CN (B, F)
$\Phi_R(G_1^+)$	d_1	0.66, 0.88	0.67, 0.93	0.67, 0.94
$\Phi_R(G_2^+)$	d_2	0.53, 0.35	0.51, 0.28	0.50, 0.26
$\Phi_{SUB}(Nu^+)$	d_3	0.40, 0.27	0.43, 0.22	0.44, 0.21
$\Phi_{ET}(Nu^+)$	d_4	0.20, 0.06	0.15, 0.00	0.15, 0.00

[a] The coefficients are determined from eqs 4–7 using PUHF charges and spin densities.

coordinate. The reactant state is dominated by the $\Phi_R(G_1^+)$–$\Phi_R(G_2^+)$ mixing which is gradually turned off and is replaced by the $\Phi_R(G_1^+)$–$\Phi_{SUB}(Nu^+)$ mixing at the product state. At all other points along the reaction coordinate, both configuration-mixing interactions are turned on, and their strength will depend on the configuration energy gaps. It follows therefore that the TS which is by definition the maximum on the potential energy curve will be located at the place where the VB stabilizing interactions are at minimum. Indeed, as seen from Figure 6, the approximate position of the TS corresponds to the crossing point of $\Phi_R(G_2^+)$ and $\Phi_{SUB}(Nu^+)$ which is precisely the geometry where their configuration energy gap with respect to $\Phi_R(G_1^+)$ is at maximum, and where consequently the stabilizing interactions are at minimum.

Solvent Effect on the Mechanism of TS Formation. Table 9 shows the VB coefficients for the frontside and backside TSs of $H_2S/C_2H_6^{\bullet+}$ at the highest common level for the gas phase and the two solvents, CH_2Cl_2 and CH_3CN. In the backside mechanism, the solvent increases the contribution of the SUB configuration at the expense of the ET configuration. This is of course a reflection of the change in the TS geometry that progresses (see Figure 4) in solution toward increasing Nu–G_1 bond making and G_1–G_2 bond breaking. Other than this feature, it is apparent from the VB coefficients that the location of the TS is still approximately at the crossing geometry (C) of the $\Phi_R(G_2^+)$ and $\Phi_{SUB}(Nu^+)$ configurations. Thus the gas phase mechanism of TS formation remains intact in solution, at least at the very simple level of solvent effect used in the present study, and *the TS is therefore the state of trade-off between the one-electron bond* $(G_1{\cdot}G_2)^+$ *and the two-electron bond* $(Nu{-}G_1)^+$ *along the reaction coordinate.*

A VB Mixing Model for the TS. Following the preceding description of TS formation, we may turn now to piece together the electronic structure of the TS from the VB building blocks, by seeking a reasonable approximation for the TS.[21] Initially we construct Φ_C, as shown in eq 10. This is the wave function that represents the bonding combination of $\Phi_R(G_2^+)$ and $\Phi_{SUB}(Nu^+)$ at their crossing point (C in Figure 6). The remaining configurations, $\Phi_R(G_1^+)$ and $\Phi_{ET}(Nu^+)$, will mix into Φ_C to generate the perfectly resonating state (PRS)[46] in eq 11a that corresponds to the final state at the crossing geometry (C). In view of the preceding discussion of the TS, the PRS may be considered as an approximate model to the TS, as expressed in eq 11b.

$$\Phi_C = 2^{-1/2}[\Phi_R(G_2^+) + \Phi_{SUB}(Nu^+)] \quad (10)$$

$$\Psi_{PRS} = d_C\Phi_C + d_1\Phi_R(G_1^+) + d_4\Phi_{ET}(Nu^+) \quad (11a)$$

$$\Psi_{TS} \approx \Psi_{PRS} \quad (11b)$$

Figure 7 is a VB mixing diagram[42] that represents pictorially the construction of Ψ_{PRS} as a model for the TS. The electronic structure of the TS results from the mixing of Φ_C and Φ_{ET} into $\Phi_R(G_1^+)$; the latter being the lowest lying configuration at the crossing point. Both mixings depend on the corresponding configuration mixing energy gaps ΔE_1 and ΔE_2 in Figure 7. Larger mixing gaps will lead to smaller VB mixings and a more dominant $\Phi_R(G_1^+)$ character in the TS. The ΔE_2 gap depends on the ionization potential of the nucleophile and the electron

(46) For the definition of the PRS of a chemical reaction, see: Truhlar, D. G. *Faraday Trans.* **1994**, *90*, 1670. Shaik, S. *Faraday Trans.* **1994**, *90*, 1671. PRS replaces the term ACS used previously (ref 21).

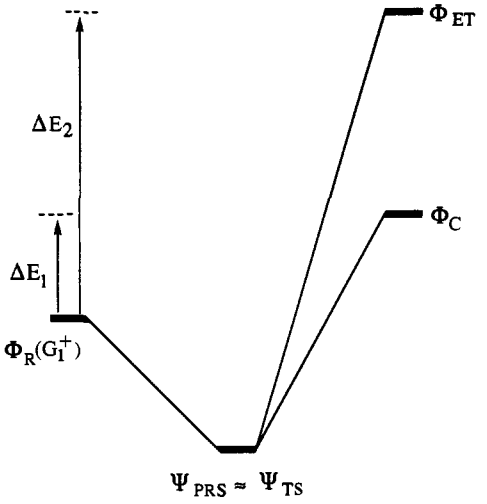

Figure 7. VB mixing diagram showing the construction of Ψ_{PRS} (eq 11) as a model for Ψ_{TS}, by the mixing of Φ_C and Φ_{ET} into $\Phi_R(G_1^+)$. Φ_C refers to the state resulting from the crossing of $\Phi_R(G_2^+)$ and Φ_{SUB}-(Nu^+), defined in eq 10. Following perturbation theoretic arguments the mixing is inversely proportional to the configuration energy gaps, ΔE_1 and ΔE_2. Both ΔE's are larger; the larger is the ionization potential of the nucleophile.

affinity of the cation radical. ΔE_1 depends on the height of the resonating combination, Φ_C, at crossing point which, in turn, is determined by the balance of $Nu^{\bullet} - {}^{\bullet}G_1$ coupling and $G_1{}^{\bullet}\,{}^{\bullet}G_2$ triplet repulsion[44] (see Discussion later).

Figure 7 can serve as a basis for understanding some of the TS features which appear in Tables 6 and 8. Consider first the backside TS for a given cation radical species. The VB mixing will depend on the ionization potential of the nucleophile, IP-(Nu:). The higher the IP, the higher are the starting points of $\Phi_{SUB}(Nu^+)$ and $\Phi_{ET}(Nu^+)$ at the reactants extreme, and the higher Φ_C and $\Phi_{ET}(Nu^+)$ will be above $\Phi_R(G_1^+)$ at the TS location. Thus, when IP(Nu:) is quite low as in *class A* (H_2S/$C_2H_6{}^{\bullet+}$), the TS will be more delocalized by VB mixing and will therefore possess a smaller positive charge on G_1 and a higher electron-transfer character, in comparison with *class B* (H_2O/$C_2H_6{}^{\bullet+}$) for which IP(Nu:) is higher. This is the origin of the patterns observed in the VB coefficients of the backside TSs in Table 8, as well as in the spin and charge density data in Table 6.

Tunring now to the frontside TSs in Table 8, it is apparent that irrespective of the classification, all the frontside TSs are characterized by a less pronounced VB mixing, and their wave function, eq 11, is dominated by $\Phi_R(G_1^+)$. The fact that this poor mixing situation persists even in *class A*, where the configuration energy gaps (Figure 7) are potentially favorable for extensive VB mixing, is an indication of some orbital symmetry constraints which prohibit the VB mixing.

C. Orbital Selection Rules: Stereospecificity of Nucleophile Substitution. To understand the orbital symmetry constraints, we need to use the VB set **1**−**4** in a slightly different *aufbau* procedure. To this end, we transform the VB configurations to representations where the electrons occupy reactant fragment MO's and are spin-paired in the VB sense (for details see in Appendix 1.B).[42] In this manner orbital symmetry becomes an inherent ingredient in the VB mixing pattern of the TS, as demonstrated before by Shaik and Dinnocenzo.[15]

The three principle VB configurations are depicted in Figure 8 in terms of reactant MO's. The first structure is the reactant configuration which is expressed above in eq 8 as the bonding linear combination of the two localized structures $\Phi_R(G_1^+)$ and $\Phi_R(G_2^+)$ and which, in Figure 8, is represented by an electron

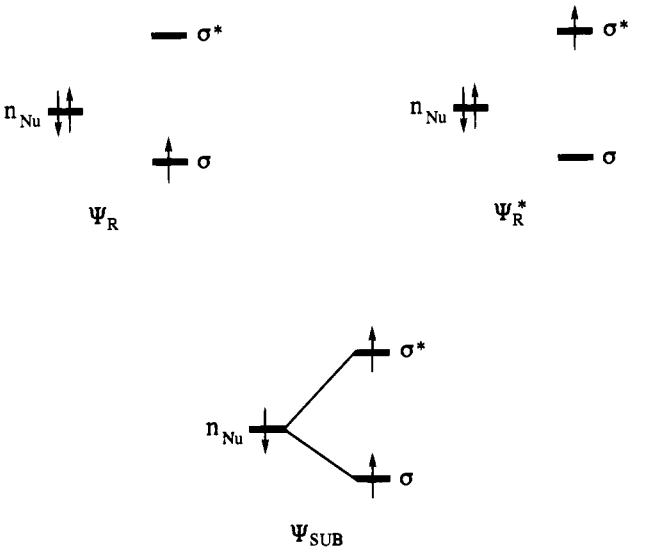

Figure 8. VB configurations based on reactant fragment MOs. The orbitals are n_{Nu} which refers to the active orbital localized on the nucleophile and the σ and σ^* active orbitals corresponding to the one electron bond of the cation radicals. The orbitals are not frozen and are adapted to the geometric changes which occur in the reactant fragments along the reaction coordinate. The ET configuration (not shown) corresponds to the $n_{NU}{}^1\sigma^2$ electron occupation.

pair in an orbital of the nucleophile (n_{NU}), and a single electron in the σ orbital of the cation radical moiety. The second configuration in Figure 8 involves a single electron in the σ^* orbital of the cation radical moiety.[47] This configuration corresponds to the anti-bonding combination of the two localized structures $\Phi_R(G_1^+)$ and $\Phi_R(G_2^+)$. The coefficients of these two group-orbital VB configurations can be determined from the coefficients (d_1 and d_2) of the localized structures in eqs 4 and 5, and the resulting expression are as follows:

$$d(\Psi_R) = 2^{-1/2}(d_1 + d_2) = 2^{-1/2}\{[Q(G_2)]^{1/2} + [Q(G_1)^{1/2}]\} \quad (12)$$

$$d(\Psi_R{}^*) = 2^{-1/2}(d_2 - d_1) = 2^{-1/2}\{[Q(G_2)]^{1/2} - [Q(G_1)]^{1/2}\} \quad (13)$$

The third configuration in Figure 8 possesses a single electron on the nucleophile and a triplet pair of electrons in the σ and σ^* orbitals of the cation radical moiety. The three electrons are coupled into a total doublet spin accounting for one singlet electron-pair bond between the nucleophile and the cation radical and one odd electron residing on the cation radical moiety. This representation of Ψ_{SUB} is related to the original $\Phi_{SUB}(Nu^+)$ configuration (**3** above). But unlike **3**, Ψ_{SUB} involves a proper spectroscopic state (made of $Nu^{\bullet+}$ and a precisely triplet $G_1{}^{\bullet}\,{}^{\bullet}G_2$ moiety) at infinite separation between Nu and the cation radical moiety.[48] The coefficient of this Ψ_{SUB} configuration is related to the coefficient of the original $\Phi_{SUB}(Nu^+)$ configuration as shown in eq 14, while the coefficient of $\Phi_{ET}(Nu^+)$ remains as in eq 7 (see Appendix 1.B).

$$d(\Psi_{SUB}) = 3^{1/2}d_3 = 3^{1/2}\{[Q(Nu) - \varrho(Nu)]^{1/2}\} \quad (14)$$

The coefficients of the reactant-orbital VB configurations in Figure 8 can be obtained from the corresponding VB configurations in Table 8 by the simple expressions spelled in eqs 12−

(47) For the use of these three configurations to describe the curve crossing situation of cation radical decomposition, see: Takahashi, O.; Kikuchi, O. *Tetrahedron Lett.* **1991**, *37*, 4933.

(48) See Appendix 1: Maitre, P.; Hiberty, P. C.; Ohanessian, G.; Shaik, S. S. *J. Phys. Chem.* **1990**, *94*, 4089.

14 and 7. It is apparent that the largest coefficients will be those of Ψ_{SUB} and Ψ_R, that will therefore dominate the resonance stabilization of the TS. Since these two configurations differ by a single-electron shift from the orbital of the nucleophile, n_{NU}, to the σ^* orbital of the cation radical, then following VB mixing rules,[42] the two configurations will interact in proportion to the overlap of these orbitals. It follows, therefore, that the resonance energy of the TS and hence also the stereochemistry of nucleophilic cleavage will be affected by the nodal properties of the σ^* orbital of the cation radical moiety and will favor thereby the backside trajectory. The role of the σ^* orbital of the cation radicals is in fact vividly apparent in the $C_3H_6^{\bullet+}$ system. In this system, the σ orbital of the long-bond has a better overlap with n_{Nu} in a frontside approach of the nucleophile, while the corresponding σ^* orbital favors a backside overlap. The computed favorable bonding in the backside TS for the Nu:/$C_3H_6^{\bullet+}$ systems is thus correlated with the overlap capability of the σ^* orbital. *The VB mixing at the TS obeys therefore a definitive orbital selection rule.*

Alongside the resonance energy of the TS, its structural deformations consistitute another important aspect of the stereoselectivity. This can be deduced from the crossing mechanism in Figure 6 between the SUB configuration and the $\Phi_R(G_2^+)$ component of Ψ_R. Since, initially the SUB configuration is an excited state of the reactants, the crossing requires the stabilization of the SUB configuration by the bonding between the nucleophile and the cation radical as well as by the loss of the triplet repulsion across the $G_1^{\bullet}$ $^{\bullet}G_2$ moiety.[44,48] The intrinsic bonding of Ψ_{SUB} in Figure 8 is proportional to the sum of overlaps of the nucleophilic orbital, n_{NU}, with the σ and σ^* orbitals of the cation radical moiety.[42,49] The consequence is a stereochemical preference for backside attack because along the backside trajectory the $n_{NU}-\sigma^*$ overlap is maximum, but the same overlap vanishes along the frontside trajectory. In the absence of a good bonding interaction for Ψ_{SUB} in the frontside approach, the requisite VB crossing for TS formation will demand much greater deformations in comparison with the backside approach. Indeed, the computed (UHF/6-31G*) deformation energies of the fragments were found to be 16.0−25.1 kcal/mol for the frontside TSs as compared with only 3.4−6.7 kcal/mol for the backside TSs. This is commensurate with the enhanced deformations of the cation radical moieties in the frontside TSs, e.g., in Figures 4 and 5, as well as from the associated discussions in the results section.

To summarize: *the computed stereospecificity in the nucleophilic substitutions is due to better resonance bonding and less deformation energy in the backside TS. These two factors are related to the interactions of the nucleophile with the σ^* orbital of the cation radical.* The combination of our computational results, VB modeling, and the experimental findings of Dinnocenzo and co-workers[6] make quite a convincing case for the decisive role of the σ^* orbital in the overwhelming backside stereospecificity of cation radical cleavage by nucleophiles.

C. Reactivity Patterns. A major trend in our computational results in Table 4 is the very small central barrier for the backside nucleophilic cleavage. For a given cation radical, the central barriers are seen to follow the order, $H_2S \approx H_2O \gg NH_3$, PH_3; where the latter two nucleophiles lead to barrierless processes. Since the question of the magnitude of the barrier in reactions between nucleophiles and cation radicals has become controversial,[10−14] and since small barriers are observed also in many of the experimental systems in the gas phase[11,14b] and in solution,[6,12,41] it becomes essential to model the barrier height and to derive simple structure−reactivity relationships that allow the computational and experimental results to be rationalized and to make predictions in some lucid and more refined manner than previously.[13] This section makes use of the VB model to achieve these goals.

Models for the Barrier Height in Nucleophilic Cleavages of Cation Radicals. The prediction of trends in the barrier height requires a more compact representation of the VB crossings shown in Figure 6. Figure 9a is a compact state correlation diagram (SCD) that describes the barrier formation for *class A* nucleophilic cleavages.[15] The basis for the state correlation is the crossing shown before in Figure 6a, typical of *class A*. Thus, the $\Phi_R(G_2^+)$ and $\Phi_{SUB}(Nu^+)$ curves define the spine of the diagram, while $\Phi_R(G_1^+)$ which participates in the bonding situations of both reactants and products (eqs 8 and 9) is mixed separately into each of the curves to complement the two ground anchor states of the diagram (see Appendix 2.A for more details). In this manner, the vertical excited state at the reactants extreme $(\Psi_{SUV})^v$ correlates with the ground state of the product by virtue of sharing the same dominant VB contribution, $\Phi_{SUB}(Nu^+)$. Similarly, the ground state of the reactants correlates with a vertical charge transfer state of the product $\Psi_P(CT)^v$ by virtue of sharing the same VB character, $\Phi_R(G_2^+)$.

In *class B*, $(\Psi_{SUB})^v$ still correlates with $\Psi_{SUB}(Nu^+)$, but now this configuration is not the dominant contributor of the product (consult Table 8). In fact, the reaction profile is dominated throughout by a single configuration, $\Phi_R(G_1^+)$, and hence a compact model like in *class A* is not useful, and the suitable model for *class B* remains the three curve VB diagram in Figure 9b. This figure is a reproduction of Figure 6b except that the anchor state $(\Psi_{SUB})^v$ is substituted for the associated configuration $\Phi_{SUB}(Nu^+)$.

The difference between the two electronic classes follow from Figure 9a,b. Thus, in *class A*, the barrier arises due to the avoided crossing of two bonding situations that interchange along the reaction coordinate. On the other hand, in *class B* the barrier arises from a single configuration, $\Phi_R(G_1^+)$, which trades off VB mixing partners along the reaction coordinate: from $\Phi_R(G_2^+)$ initially to $\Phi_{SUB}(Nu^+)$ finally. Reactivity patterns are likely to reflect the different origins of barrier formation.

Barriers Heights in *Class A*. Equation 15 provides an expression for the central barrier that is based on Figure 9a. It has been derived in detail in a recent monograph[5e] and has already been used in the primary literature:[50]

$$\Delta E_C^{\ddagger} = \Delta E_{CROSS} - B$$

$$\Delta E_{CROSS} = [(f_R + f_P)G_R + (1 - f_R - f_P)\Delta E_{RP}]\{(G_P + \Delta E_{RP})/(G_R + G_P)]\} \quad (15)$$

Here ΔE_{CROSS} is the height of the crossing point given as a function of the vertical excitation gaps of the diagram at the reactant (G_R) and product (G_P) extremes, the reaction energy change, ΔE_{RP}, and of f_R and f_P which are curvature parameters of the reactant and product curves, respectively. B is the avoided crossing resonance energy of the TS.

To treat the Nu/$C_3H_6^{\bullet+}$ systems, for which Gp values are difficult to obtain, eq 15 should be further simplified by expansion of the term in brackets as follows in eq 16.

(49) Following the approximate VB theory described in ref 42, the bonding interaction in $(\Psi_{SUB})^v$ is given by the sum of $(2hs)_{n_{Nu}\sigma}$ and $(2hs)_{n_{Nu}\sigma^*}$, where h is the reduced resonance integral and s is the corresponding overlap integral, with respect to the orbitals indicated in the subscript.

(50) Apeloig, Y.; Aharoni, O.-M.; Danovich, D.; Ioffe, A.; Shaik, S. *Isr. J. Chem.* **1993**, *33(4)*, 387.

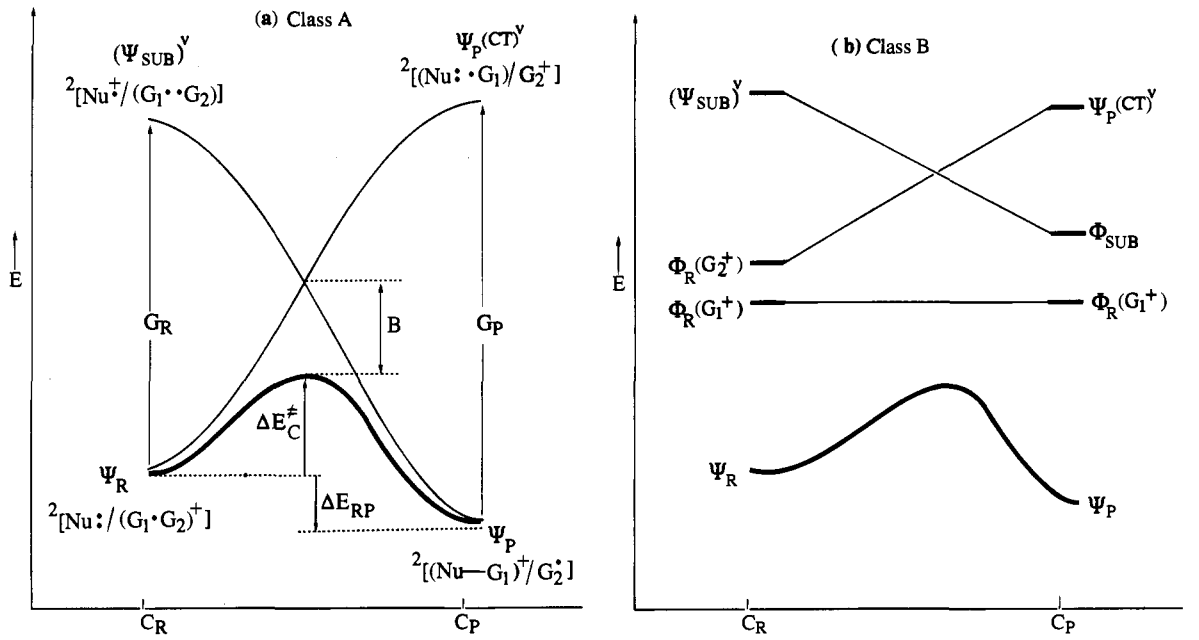

Figure 9. Models for barrier formations in (a) *class A* (a case of a good donor acceptor pair) and in (b) *class B* (a case of a poor donor acceptor pair) nucleophilic cleavage mechanisms. The diagram extremes refer to the clusters. (a) State correlation diagram showing the barrier formation in *class A* as a result of an avoided crossing. The avoided crossing is shown by the thicker line. B is the corresponding resonance energy due to avoided crossing. The G_R and G_P are vertical gaps. The electron dot cartoons describe the states at infinite fragment separation. (b) VB mixing diagram showing the formation of the barrier in *class B* due to the exchange of VB interaction partners by the $\Phi_R(G_1^{+})$ along the reaction coordinate.

$$(G_P + \Delta E_{RP})/(G_R + G_P) = 0.5 + 0.5(G_P - G_R + 2\Delta E_{RP})/(G_R + G_P) \quad (16)$$

The second term in eq 16 is small, unless the reaction is very exothermic or endothermic and at the same time possesses approximately equal vertical gaps, $G_R \approx G_P$.[51] Neglect of the second term in eq 16 converts the barrier expression in eq 15 to eq 17.

$$\Delta E_C^{\ddagger} \approx 0.5(f_R + f_P)G_R + 0.5(1 - f_R - f_P)\Delta E_{RP} - B \quad (17)$$

The curvature factors f_R and f_P in eqs 15 and 17 are related to the bond-coupling capabilities of the excited states[5c,e,14a] in the diagram as well as to electrostatic,[52] steric and exchange repulsion effects[48,53] in the respective ground states. For the simple cation radicals of the present study these factors do not play a major role, and we may assume the quadratic approximation for the curves, where the f_R and f_P are both 0.25. The barrier expressions in eqs 15 and 17 are then simplified to eqs 18 and 19, respectively.

$$\Delta E_C^{\ddagger} = 0.5(G_R + \Delta E_{RP})\{(G_P + \Delta E_{RP})/(G_R + G_P)\} - B \quad (18)$$

$$\Delta E_C^{\ddagger} \approx 0.25(G_R + \Delta E_{RP}) - B \quad (19)$$

The simplified eqs 18 and 19, can be utilized to estimate barriers in the *class A* reactions of $C_2H_6^{\bullet+}$ and $C_3H_6^{\bullet+}$ by inputting vertical gaps, reaction energies, and TS resonance interactions. The vertical gaps and reaction energies can be estimated at the UHF/6-31G* level and are shown in Table 10 for the reactions of $C_2H_6^{\bullet+}$. For the reactions of $C_3H_6^{\bullet+}$, we presently have only G_R and ΔE_{RP} data because variational collapse of the charge transfer wave function did not enable us to compute the Gp gap. Using these raw data in eqs 18 and 19, it is possible to calculate the heights of the crossing points for the *class A* reactions.

It is seen that H_2S possesses the highest crossing point, while the NH_3 and PH_3 nucleophiles possess much lower crossing points. These trends reflect the tendencies in the corresponding barriers of the *class A* reactions, H_2S > NH_3, PH_3, for either the backside or the frontside varieties. The heights of the crossing points in entries 1−5 in Table 10 are seen to be quite small, so that an avoided crossing resonance interaction of moderate size will lead to small barriers for the backside nucleophilic cleavage reactions.

The resonance interaction can be estimated in several ways based on the overlap between the active orbital of the nucleophile and the σ^* orbital of the G_1-G_2 moiety in the TS (see Appendix 2.B). Using different approaches for the reaction of H_2S with $C_2H_6^{\bullet+}$ leads to a value of ≈20 kcal/mol for the backside TS and ≈6 kcal/mol for the frontside TS. Assuming that the above B values carry over to other reactions, we obtain the barrier heights in entries 1−5 in Table 10, where a negative barrier height means *a barrierless process*.[50,54]

It can be seen that the simple model equations (eqs 18 and 19) predict the general trends of the computational study. Firstly, frontside barriers are consistently larger than backside barriers due to the much smaller B value which is dominated by the σ^* orbital.[55] Secondly, the calculated barriers for the backside reactions of $C_2H_6^{\bullet+}$ are very small (for H_2S in entry 1) or absent (entries 2 and 3). Finally, even though eq 19 overestimates barriers in comparison with eq 18, the backside barriers for $C_3H_6^{\bullet+}$ are still small. All of these features are in general accord with the computed data, and we conclude that

(51) This approximation was checked on the large S_N2 data set in ref 5e (Table 6.10 there) as well as on reactions of cation radicals in solution and was found to be satisfactory. For the cases treated here, the approximation is very good for H_2O and NH_3 and will overestimate barriers for H_2S and more so for PH_3. We are therefore assured that the use of eq 19 will not artificially underestimate barriers.

(52) Sini, G.; Shaik, S. S.; Hiberty, P. C. *J. Chem. Soc., Perkin Trans. 2* **1992**, 1019.

(53) Shaik, S. S.; Hiberty, P. C.; Ohanessian, G.; Lefour, J. M. *J. Phys. Chem.* **1988**, *92*, 5086.

(54) See discussions of negative barriers obtained with eq 18 in ref 5e, p 240, and in ref 50.

Table 10. Reactivity Factors[a] for *Class A* Reactions (Figure 9a) and Calculated Barriers

entry	Nu/cation radical	*Class*	G_R	G_P	ΔE_{RP}	ΔE_{CROSS}[b]	$\Delta E_c^{\ddagger}$ (B)[c]	$\Delta E_c^{\ddagger}$ (F)	$\Delta E_c^{\ddagger}$ (B) (6-31G*)[f]
1	$H_2S + C_2H_6^{\bullet+}$	*A*	120.0	149.9	−27	21.2, 23.3	1.2, 3.3	15.2[d]	0.5
2	$NH_3 + C_2H_6^{\bullet+}$	*A*	119.8	241.8	−61	14.7, 14.7	−5.4, −5.3	8.7[d]	<0
3	$PH_3 + C_2H_6^{\bullet+}$	*A*	121.8	157.9	−54	12.6, 17.0	−7.4, −3.0	6.6[d]	<0
4	$H_2S + C_3H_6^{\bullet+}$	*A*	121.6		−20	25.3	5.3	19.3[e]	1.3
5	$NH_3 + C_3H_6^{\bullet+}$	*A*	119.9		−56	16.0	−4.0	10.0[e]	<0
6	$H_2O + C_2H_6^{\bullet+}$	*B*	157.1	223.5	−23	35.3, 33.5[g]			0.3
7	$H_2O + C_3H_6^{\bullet+}$	*B*	158.2		−20	34.6[g]			1.1
8	$H_2S + Si_2H_6^{\bullet+}$	*B*	129.8	119.9	−14	24.6, 29.0[g]			<0

[a] In kcal/mol. The *G* values are vertical gaps. ΔE_{RP} is the reaction energy. [b] Refer to the term preceding B in eqs 18 and 19. The first value in each entry is calculated using eq 18. The second value is calculated using eq 19. The same trends are obtained if the computed G_R values are corrected to account for the experimental IPs of the nucleophiles. [c] Calculated using eq 18 (the first value) and eq 19 (the second value). $B = 20$ kcal/mol (Appendix 2). Negative results means a barrierless process. [d] Calculated using eq 18. $B = 6$ kcal/mol (Appendix 2). [e] Calculated using eq 19. $B = 6$ kcal/mol (Appendix 2). [f] UHF/6-31G* From Table 4. The negative barrier in entries 2, 3, and 8 refers to the barrierless processes discussed in the Results section. [g] Calculated crossing points as if these reactions were *Class A* types.

Table 11. Computed[a] Kinetic Isotope Effects for the Process R (Reactants) → TS (Transition State), for *Class A* and *Class B* Reactions in the Backside and Frontside Mechanism

entry	reaction[b]		G_1-D[c]	G_2-D[c]	G_1G_2-D[c,d]	$Nu-D$[e,f]
			Class A			
1a	$H_2S + C_2H_6^{\bullet+}$	B	0.596 (0.646)	1.131 (1.114)	0.676 (0.720)	0.811 (0.842)
1b		F	1.171 (1.157)	1.593 (1.484)	1.873 (1.721)	0.897 (0.916)
2a	$H_2S + C_3H_6^{\bullet+}$	B	0.763 (0.797)	1.201 (1.170)	0.916 (0.932)	0.873 (0.899)
2b		F	0.960 (0.969)	1.494 (1.405)	1.433 (1.362)	0.899 (0.915)
3a	$NH_3 + C_3H_6^{\bullet+}$	F	0.859 (0.879)	1.344 (1.284)	1.155 (1.131)	0.810 (0.848)
			Class B			
4a	$H_2O + C_2H_6^{\bullet+}$	B	0.581 (0.629)	1.325 (1.273)	0.770 (0.800)	0.957 (0.976)
4b		F	1.135 (1.125)	1.653 (1.530)	1.882 (1.725)	0.954 (0.971)
5a	$H_2O + C_3H_6^{\bullet+}$	B	0.722 (0.753)	1.339 (1.270)	0.948 (0.957)	0.935 (0.999)
5b		F	0.953 (0.940)	1.480 (1.385)	1.361 (1.301)	0.912 (0.976)

[a] UHF/6-31G*. In parentheses are values scaled by 0.8929. [b] B is backside; F is frontside. [c] G_1-D refers to the replacement of the G_1 hydrogens by deuteriums. G_2-D refers to the G_2 hydrogens, while G_1G_2-D refers to the replacement of all the G_1 and G_2 hydrogens by deuteriums. [d] There is also a small isotope effect for the H → D replacement in the central CH_2 group in $C_3H_6^{\bullet+}$. [e] *Nu-D* refers to the replacement of the H's on the nucleophile to deuteriums. [f] The heavy atom isotope effects on C and on Nu are very small.

eqs 18 and 19 may together constitute a tool to analyze reactivity patterns in *class A* reactions.

Barrier Heights in *Class B*. Entries 6 and 7 in Table 10 contain the parameters for the reactions of H_2O with $C_2H_6^{\bullet+}$ and $C_3H_6^{\bullet+}$ which belong to *class B*. It is seen that despite the unfavorable parameters (e.g., the large G_R) these backside reactions nonetheless possess very small barriers (see last column). A similar situation is found for the third reaction of *class B*, H_2S with $Si_2H_6^{\bullet+}$ (entry 8), which is a barrierless process despite the unfavorable parameters. It is here where we see the fundamental distinction that is rooted in the different mechanisms of barrier formation in the two classes. Thus, *class B* reactions will not fall into the same structure reactivity patterns of *class A*. As seen in Figure 9b, the source of the small backside barrier of the *class B* reactions of H_2O with $C_2H_6^{\bullet+}$ and $C_3H_6^{\bullet+}$ is the dominance of the entire potential energy profile by the lowest lying VB configuration. This uniconfigurational dominance will generally result in a small barrier provided two conditions are met: (a) the VB mixing along the reaction coordinate is favorable and (b) the reaction is exothermic. Since all the reactions of *class B* in entries 6–8 are exothermic and possess a significant VB mixing in the backside trajectory, they all possess very small barriers. The effect of poor VB mixing is reflected in the high frontside barriers of *class B* reactions (see Table 4).

Why Are the Computed Activation Barriers so Small for Nucleophilic Cleavage of Cation Radicals? The analysis of the barriers in Table 10 reveals that the small barriers for the backside cleavages can be traced to two factors. In *class A*, it is the combination of exothermicity that leads to a low energy crossing point and the significant avoided crossing resonance interaction that finally results in a very low barrier or in a barrierless process. In *class B*, both the reaction exothermicities and the significant VB mixing in the TS region result in low barriers. Thus, while the two classes are expected to exhibit distinct structure–reactivity patterns, the major causes of the small barriers in both cases are closely related.

D. Kinetic Isotope Probes for Stereochemistry and the Electronic Structure of the TS. While the VB notions of TS structure and electronic classification are conceptually useful and theoretically verifiable, they still require an observable probe that can be tested experimentally. We have calculated isotope effects for the several reactions in order to determine their potential applicability. Table 11 shows isotope effect calculations for a few of the target reactions for the backside and frontside stereochemical pathways. In each case, the isotope effects refer to the process R → TS and involve a few possible combinations of isotopic labeling on the cation radical and on the nucleophiles in the $Nu-G_1-G_2^+$ species. The values out of parentheses are unscaled isotope effects, while the parenthetical values are scaled by the default factor of 0.8929.[26]

Inspection of the data in Table 11 shows that the isotope effect arising from the replacement of the hydrogens on G_1 by deuteriums, G_1-D, provides a probe of stereochemistry. The G_1-D value is strongly inverse (<1) for the backside TS and normal or closely so (≥1) for the frontside TS. These values reflect the bonding characteristics of the respective TSs as predicted by the VB analysis. Thus, the inverse G_1-D value of the backside mechanism indicates that the central G_1 group in the backside TS is strongly bonded by the nucleophile as well as by the leaving group G_2. On the other hand, the normal G_1-D for the frontside TS is a consequence of the weak Nu–G_1 and G_1-G_2 bonding interactions. Moreover, the normal

G_1-D is also a probe of the severe tilt deformation of the G_1 group in the frontside TS (see the HC_1C_2 angle β in Figure 3 and 4). Thus, the *G_1-D isotope effect should be a useful probe of the orbital symmetry and deformation effects that characterize the bonding features of the backside and frontside TSs.*

The *Nu−D* isotope effect could potentially provide a probe for the electronic structure of the TSs. As may be seen, this quantity is slightly smaller than unity for the backside reactions of *class A* and close to unity in the backside reactions of *class B*. While these values reflect bonding differences between the two reaction types, we do not think they are sufficiently different to provide an unambiguous experimental probe. Therefore, other methods will have to be developed to distinguish these reaction types.

Concluding Remarks

This work develops the means to conceptualize and predict reactivity patterns for nucleophilic substitution reactions on σ-cation radicals by a combination of ab initio computations and their modeling by VB mixing ideas. The resulting analysis provides insight into the electronic structure and bonding in the TS, into the origins of TS formation, and into the origins of the barriers and stereospecificity of nucleophilic substitution reactions of σ-cation radicals.

The stereochemistry of nucleophilic substitution is shown to follow a definitive orbital selection rule and be governed by the σ^*(LUMO) orbital of the cation radical. It was also shown that for cation radicals whose stereochemistry would be difficult to elucidate by classical methods (e.g. $C_3H_6^{\bullet+}$), secondary deuterium isotope effects may serve as a more convenient experimental probe.[56]

Two electronic classes of substitution emerge from the ab initio computations and the VB analysis, *class A* and *class B*, which differ in the extent of charge and spin delocalization in the respective TSs. The difference between the two classes is associated with the different nature of the corresponding electron-pair bonding in $Nu-G_1^+$. *Class A* reactions involve nucleophile/cation radical combinations where the $Nu-G_1^+$ bond wave function is dominated by the spin-paired HL configuration. In contrast, *class B* reactions are cases where the $Nu-G_1^+$ bond wave function is dominated by the Nu: G_1^+ structure, much like the "dative" bonds between ligands and positive metal centers. These differences are expressed in the corresponding low energy TSs; the *class A* TS possesses roughly an evently distributed positive charge over the $(Nu^{\bullet\bullet}G_1^{\bullet\bullet}G_1)^+$ structure, while the *class B* TS has an appearance of a cationic central group, G_1^+, coordinated by dative bonds to Nu:, on one side, and to $G_2^{\bullet}$, on the other side. Based on these differences, we suggest that the terms "homopolar" and "heteropolar" may serve as appropriate descriptors of *class A* and *class B* reactions, respectively.

There remain quite a few unsettled problems related to the clear assignment of the electronic class for a given reactant pair, the limitations of the classification scheme, and the possible borderline cases involving transitions between homopolar and heteropolar reactivity. These, as well as the extension of the VB modeling to more complex systems, are major challenges for the future.

Appendixes

Appendix 1: VB Configurations. A. Properties of the Model VB Wave Function. Equation A1.1 describes a wave function that accounts for the disparity between the group spin and charge densities on Nu (nucleophile) by mixing $\Phi_{SUB}(Nu^+)$ and $\Phi_{ET}(Nu^+)$. The normalization constant (with neglect of differential overlap)[42] in eq A1.1 follows from the Slater determinant expressions of the $\Phi_{SUB}(Nu^+)$ and $\Phi_{ET}(Nu^+)$ wave functions in eqs A1.2 and A1.3 where the ω and $\bar{\omega}$ are spin group-orbitals with spin-up and spin-down, respectively, and extend over the spatial part indicated by the subscript. The remaining VB structures correspond to eqs A1.4 and A1.5.

$$\Phi(Nu^+) = (1 + \lambda + \lambda^2)^{-1/2}[\Phi_{SUB}(Nu^+) + \lambda\Phi_{ET}(Nu^+)] \quad (A1.1)$$

$$\Phi_{SUB}(Nu^+) = 2^{-1/2}[|\omega_{Nu}\bar{\omega}_{G_1}\omega_{G_2}| - |\bar{\omega}_{Nu}\omega_{G_1}\omega_{G_2}|] \quad (A1.2)$$

$$\Phi_{ET}(Nu^+) = 2^{-1/2}[|\omega_{Nu}\bar{\omega}_{G_1}\omega_{G_2}| - |\omega_{Nu}\omega_{G_1}\bar{\omega}_{G_2}|] \quad (A1.3)$$

$$\Phi_R(G_1^+) = |\omega_{Nu}\bar{\omega}_{Nu}\omega_{G_2}| \quad (A1.4)$$

$$\Phi_R(G_2^+) = |\omega_{Nu}\bar{\omega}_{Nu}\omega_{G_1}| \quad (A1.5)$$

The linear combination of $\Phi(Nu^+)$ with the latter two wave functions leads to eq A1.6 from which follow eqs A1.7−A1.13 for charge and spin densities:

$$\Psi = N[\Phi(Nu^+) + a_1\Phi_R(G_1^+) + a_2\Phi_R(G_2^+)]; \quad N = (1 + a_1^2 + a_2^2)^{-1/2} \quad (A1.6)$$

$$Q(Nu) = (1 + a_1^2 + a_2^2)^{-1} \quad (A1.7)$$

$$Q(G_1) = a_1^2 Q(Nu) \quad (A1.8)$$

$$Q(G_2) = a_2^2 Q(Nu) \quad (A1.9)$$

$$\varrho(Nu) = Q(Nu)[(\lambda + \lambda^2)/(1 + \lambda + \lambda^2)] \quad (A1.10)$$

$$\varrho(G_1) = Q(Nu)[a_2^2 - \lambda/(1 + \lambda + \lambda^2)] \quad (A1.11)$$

$$\varrho(G_2) = Q(Nu)[a_1^2 + (1 + \lambda)/(1 + \lambda + \lambda^2)] \quad (A1.12)$$

$$\lambda = -0.5 + 0.5\{[Q(Nu) + 3\varrho(Nu)]/[Q(Nu) - \varrho(Nu)]\}^{1/2} \quad (A1.13)$$

Using the expression for λ (eq A1.13) we obtain the following relationships between the group charges (Q) and spin densities (ϱ) of the $Nu-G_1-G_2$ reaction complex along the reaction coordinate:

$$\varrho(G_1) = Q(G_2) - \lambda[Q(Nu) - \varrho(Nu)] \quad (A1.14)$$

$$\varrho(G_2) = Q(G_1) + (1 + \lambda)[Q(Nu) - \varrho(Nu)] \quad (A1.15)$$

Equations A1.13−A1.15 are used to test the consistency of the wave function Ψ in eq A1.6. First we use Q(Nu) and ϱ(Nu) as input in eq A1.13 to obtain λ. This λ value along with one pair of charge and/or spin density data are used as input into eqs A1.14 and A1.15, which thereby provide the predictions for the missing pair of data. For example, using in eqs A1.14 and A1.15 PQCISD(T) values for $\varrho(G_1)$ and $\varrho(G_2)$ of $H_2S/C_2H_6^{\bullet+}$ TS, we obtain the values $Q(G_1) = 0.3832$ and $Q(G_2) = 0.2927$ that compare very nicely with the PQCISD(T) values of 0.3835 and 0.2924, respectively. Similarly, using the values of $Q(G_1)$ and $Q(G_2)$ as input data, we are led to $\varrho(G_1) = 0.1984$ and $\varrho(G_2) = 0.6953$, while the corresponding PQCISD(T) results are 0.1990 and 0.6593. Similar tests for $H_2O/C_2H_6^{\bullet+}$ and other systems as well as for the other critical points (clusters) along the reaction coordinate gave the same excellent fit.

Manipulation of the eqs A1.10−A1.12 to eliminate explicit λ terms and to substitute the a_1^2 and a_2^2 by their expressions in eqs A1.8 and A1.9 leads to the equality in eq A1.16.

$$[\varrho(G_2) - Q(G_1)][Q(G_2) - \varrho(G_1)] = \varrho(Nu)[Q(Nu) - \varrho(Nu)] \quad (A1.16)$$

This equality along with eqs A1.8−A1.12 form the basis for eqs 4−7 in the text. We note that since there are more equations (A1.7−A1.12) than unknowns (λ, a_1 and a_2) one can derive three other sets of expressions that are equivalent to eqs 4−7 in the text.

B. VB Configurations in Terms of Reactant MOs. The VB configurations in Figure 8 possess electrons in reactant orbitals that are spin-paired in the VB sense.[42] The reactant orbitals are the σ and σ^* orbitals of the G_1-G_2 fragment, at any given geometry of this fragment, and the corresponding orbital on the nucleophile, ω_{Nu}. The expressions are as follows:

$$\Psi_R = |\omega_{Nu}\bar{\omega}_{Nu}\sigma| = 2^{-1/2}[|\omega_{Nu}\bar{\omega}_{Nu}\omega_{G_2}| + |\omega_{Nu}\bar{\omega}_{Nu}\omega_{G_1}|] \quad (A1.17)$$

$$\Psi_R^* = |\omega_{Nu}\bar{\omega}_{Nu}\sigma^*| = 2^{-1/2}[|\omega_{Nu}\bar{\omega}_{Nu}\omega_{G_1}| - |\omega_{Nu}\bar{\omega}_{Nu}\omega_{G_2}|] \quad (A1.18)$$

$$\Psi_{SUB} = 6^{-1/2}\{2|\bar{\omega}_{Nu}\sigma\sigma^*| - |\omega_{Nu}\bar{\sigma}\sigma^*| - |\omega_{Nu}\sigma\bar{\sigma}^*|\} = 6^{-1/2}\{2|\bar{\omega}_{Nu}\omega_{G_1}\omega_{G_2}| - |\omega_{Nu}\bar{\omega}_{G_1}\omega_{G_2}| - |\omega_{Nu}\omega_{G_1}\bar{\omega}_{G_2}|\} \quad (A1.19)$$

The coefficients of Ψ_R and Ψ_R^* in eqs 12 and 13 in the text result from the linear combination of the corresponding two localized configurations. The coefficient of Ψ_{SUB} in eq 14 in the text is related to the coefficient of Φ_{SUB} by the ratio of the corresponding normalization constants in eqs A.1.2 and A1.19.

Appendix 2: Notes on State Correlation Diagrams. A. Generation of the State Correlation Diagram for *Class A*. The construction of the state correlation diagram (SCD) in Figure 9a follows the footsteps of ref 52. There (and elsewhere, e.g., ref 5), for reactions which involve electron-pair bonding in reactants and products, the SCD is built from the reactant and product HL configurations which form the spine-curves. This spine is then dressed with all *bridging configurations. Bridging configurations are those which participate in both reactant's and product's bonding and can thereby mix individually into each one of the spine-curves to form two state-anchored-curves.* In the present case, of nucleophilic cleavage of one electron bonds, it is the $\Phi_R(G_1^+)$ structure that participates in the bonding situations of both reactants and of products and thereby qualifies as a bridging configuration. The spine of the SCD is constructed from the configurations, $\Phi_R(G_2^+)$ and $\Phi_{SUB}(Nu^+)$. We can therefore mix the bridging structure $\Phi_R(G_1^+)$ into the two spine-curves and generate in this manner two state-anchored-curves as drawn in Figure 9a for *class A*.

In *class A* nucleophilic cleavages of one electron bonds, the principal curve which emanates from the products is always $\Phi_{SUB}(Nu^+)$ which will therefore correlate with the $(\Psi_{SUB})^v$ state. However, since the reactant state is made up of two principal configurations, $\Phi_R(G_1^+)$ and $\Phi_R(G_2^+)$, the curve which emanates from the reactants dissolves eventually into two different excited states at the product extreme. Thus, $\Phi_R(G_2^+)$ correlates with $\Psi_P(CT)^v$ as in Figure 9a, while $\Phi_R(G_1^+)$ correlates with the excited state that corresponds to the antibonding combination of eq 8 in the text. This latter excited state is expressed here in eq A2.1a, and a specific example, for the $H_2S/C_2H_6^+$ case, is given in eq A2.1b.

$$\Psi_P^* = d_3\Phi_R(G_1^+) - d_1\Phi_{SUB}(Nu^+) \quad (A2.1a)$$

$$d_1 = [Q(G_1)]^{1/2}, \quad d_3 = [Q(Nu)]^{1/2}$$

$$\Psi_P^* = 0.901\Phi_R(G_1^+) - 0.435\Phi_{SUB}(Nu^+) \quad (A2.1b)$$

The two excited states, Ψ_P^* and $\Psi_P(CT)^v$ are separated only at the product extreme and are mixed in all other points (due to the mixing of the $\Phi_R(G_2^+)$ and $\Phi_R(G_1^+)$ configurations) along the reaction coordinate. Our calculations of Ψ_P^* show that it lies invariably higher than the $\Psi_P(CT)^v$ state used in Figure 9a. The corresponding G_P gap values for the Ψ_P^* state (calculated at the UHF/6-31G* level) for the $Nu/C_2H_6^{\bullet+}$ reactions are, 199.8, 424.3, 257.7, and 380.2 kcal/mol for Nu = H_2S, H_3N, H_3P, and H_2O, respectively. These gaps are higher than the charge transfer gaps in Table 10, but their trends are qualitatively identical. The lower charge transfer states justify therefore their use in Figure 9a. Practically speaking, the only difference this excited state would make is the choice of G_P value that should be used in eqs 17 and 18 to model the barrier height.

B. Estimation of the Avoided Crossing Interaction. The avoided crossing interaction was estimated by two methods. The first method used the approximation in eq A2.2 by Plato et al.[57] which proved very successful for estimating avoided crossing interactions in electron transfer reactions.

$$B = KS; \quad K = 8.8 \text{ eV}; \quad S = \langle\omega_{Nu}|\sigma^*\rangle \quad (A2.2)$$

Here S is the overlap integral between the lone pair or p orbital of the nucleophile (ω_{Nu} in eq A2.2) and the σ^* orbital of the cation radical. The overlaps, for the $H_2S/C_2H_6^{\bullet+}$ case calculated with Slater orbitals, are 0.112 for the backside TS and 0.031 for the frontside TS. Using these overlaps the B values are ~23 kcal/mol for the backside TS and ~6 kcal/mol for the frontside TS.

The second method, due to Kertesz et al.[58] is based on orbital mixing at resonance (see Bally[59]) and utilizes Extended Huckel (EH) to obtain the effective resonance integral,

$$B = -(H - E_{av}S)/(1 + S); \quad H = \langle\omega_{Nu}|\mathbf{H}|\sigma^*\rangle \quad (A2.3)$$

where H is the resonance integral and S the overlap integral of the two interacting orbtials. E_{av} is the average energy of the interacting orbitals. Using the EH approximation for H ($H = 1.75E_{av}S$) one obtains the final expression for B:

$$B = -0.75E_{av}S/(1 + S); \quad E_{av} = [E(\omega_{Nu}) + E(\sigma^*)]/2 \quad (A2.4)$$

Using the orbital energies and overlaps for the p AO of H_2S and the σ^* orbital of $C_2H_6^{\bullet+}$ leads to the $B \sim 19$ kcal/mol for

(55) For frontside pathways, the f values should be larger than the corresponding values for the backside, because the bonding interaction in $(\Psi_{SUB})^v$ is weaker relative to the backside case, and the crossing point is therefore higher in energy. Thus, the frontside barriers calculated with eq 18 are lower limits. Using the computed frontside barrier for $H_2S/C_2H_6^{\bullet+}$ as an example, one obtains that the ratio of sum of f_R and f_P (eq 17) for frontside relative to backside is 1.3.

(56) Consider, for example, $C_2H_6^{\bullet+}$. A resolution of the G_1-D and G_2-D values can be achieved by measuring the isotope effect for $C_2D_6^{\bullet+}$ as well as for $C_2D_3H_3^{\bullet+}$.

(57) Plato, M.; Mobius, K.; Michel-Beyerle, M. E.; Bixon, M.; Jortner, J. *J. Am. Chem. Soc.* **1988**, *110*, 7279.

(58) El-Shall, M. S.; Kafafi, S. A.; Meot-Ner, M.; Kertesz, M. *J. Am. Chem. Soc.* **1986**, *108*, 4391.

(59) Bally, T. In *Radical Ionic Systems*; Lund, A., Shiotani, M., Eds.; Kluwer Publ.: The Netherlands, 1991; pp 3−54.

the backside TS and $B \sim 6$ kcal/mol for the frontside TS. It was decided therefore to use average B values of ~20 and 6 kcal/mol, respectively, for the backside and frontside TSs. These B values are used in Table 10 in the text.

Acknowledgment. The research at the Hebrew University was supported by an ISF grant administered by the National Academy of Sciences and Humanities. Research at the University of Rochester was supported by the National Science Foundation (CHE-9312460) and by the donors of the Petroleum Research Foundation, administered by the American Chemical Society.

Supplementary Material Available: GAUSSIAN archive information for all the species discussed in this study (19 pages). This material is contained in many libraries on microfiche, immediately follows this article in the microfilm version of the journal, and can be ordered from the ACS; see any current masthead page for ordering information.

JA9412317